Contributions to Mineralogy and Petrology (2020) 175:113
https://doi.org/10.1007/s00410-020-01753-6

ORIGINAL PAPER

Controls on development of different mineral assemblages in gabbro and basalt during subduction metamorphism

Patricia Kang[1] · Katherine F. Fornash[2] · Donna L. Whitney[1]

Received: 13 May 2020 / Accepted: 20 October 2020 / Published online: 11 November 2020

Abstract

Coexisting fine-grained (meta-volcanic) and coarse-grained (meta-plutonic) mafic rocks in a high-pressure (P)/low-temperature (T) complex (Sivrihisar, Turkey) preserve different prograde, peak, and retrograde mineral assemblages, providing an opportunity to evaluate controls on mineral assemblages in metabasites that experienced the same P–T conditions. Fine-grained metabasalts are garnet-bearing lawsonite blueschist and eclogite with similar assemblages that vary on a mm- to cm- scale in mode of glaucophane vs. omphacite. In contrast, metagabbro consists of a disequilibrium mineral suite of relict igneous clinopyroxene partially replaced by omphacite or hydrous phases (lawsonite + tremolite or glaucophane) in a matrix of fine-grained lawsonite, omphacite, tremolite, white mica, very rare garnet, and retrograde minerals (e.g., epidote, albite, and titanite), with later chlorite and calcite. Pseudosection modeling predicts similar peak P–T conditions (490–530 °C, 1.8–2.0 GPa) for both glaucophane-rich (blueschist) and omphacite-rich (eclogite) layers of the metabasalt and similar to slightly higher conditions (490–600 °C, 1.9–2.5 GPa) for metagabbro. The range of modelled H_2O content at peak P–T conditions in metabasalt (2.0–5.4 wt%) is significantly lower than in metagabbro (6.4–8.7 wt%) due to the higher modal abundance of hydrous minerals in the latter. At the relatively similar peak P–T conditions, metagabbro experienced different reaction histories from coexisting metabasalt, thereby developing distinctive HP/LT mineral assemblages and modes (e.g., scarce garnet) owing to its more Mg-rich bulk composition ($X_{Mg} = 0.58–0.84$ vs. 0.50), higher H_2O content, and coarser grain-size. This study is the first petrologic analysis of Sivrihisar metagabbro and the first systematic study of H_2O content in metabasites from this locality, which is one of the best-preserved examples of lawsonite eclogite and blueschist in the world.

Keywords Blueschist · Lawsonite · Eclogite · Metabasalt · Metagabbro · Subduction · Turkey

Introduction

Basalt and gabbro represent different parts of an oceanic crustal section. Both experience a metamorphic transformation into blueschist and eclogite during subduction, and this transformation is controlled by various factors. The role of H_2O has been emphasized because of its catalytic effect on triggering metamorphic transformation, especially within dry, coarse-grained protoliths (e.g., Hacker 1996; Rubie 1998; John and Schenk 2003). Alongside the influence of H_2O, metabasite can preserve variable proportions of metamorphic phases and/or igneous relics depending on the bulk-rock composition of the protolith (Sandrone et al. 1986; Pognante and Kienast 1987; Pognante 1991; Gomez-Pugnaire et al. 1997; Vitale Brovarone et al. 2011; Wei and Clarke 2011). Deformation is another factor that controls the process of metamorphic transformation, because it facilitates faster reaction rates (e.g., Brodie and Rutter 1985; De Ronde and Stünitz 2007). Thus, subducted mafic high-pressure/low-temperature (HP/LT) rocks may vary in their metamorphic assemblages and reaction textures owing to the complex interplay among these controlling factors during subduction and exhumation.

Communicated by Daniela Rubatto.

Electronic supplementary material The online version of this article (https://doi.org/10.1007/s00410-020-01753-6) contains supplementary material, which is available to authorized users.

✉ Patricia Kang
kangx691@umn.edu

[1] Department of Earth and Environmental Sciences, University of Minnesota, Minneapolis, MN 55455, USA

[2] Department of Geological Sciences, Ohio University, Athens, OH 45701, USA

Some coexisting metagabbro and metabasalt that originated from oceanic crust preserve similar HP/LT mineral assemblages (Meyer 1983; Fry and Barnicoat 1987; Federico et al. 2007; Angiboust et al. 2009), but in the other cases, juxtaposed metagabbro and metabasalt consist of different mineral assemblages (Lardeaux et al. 1987; Pognante and Kienast 1987; Katzir et al. 2000; Angiboust et al. 2012). Possible explanations for the different assemblages are that the metabasalt and metagabbro (1) experienced different P–T conditions during subduction or (2) experienced the same P–T conditions but (a) differ owing to differences in bulk composition (including H_2O) and/or (b) differ owing to the effect of grain size and/or deformation on mineral reactions. Determining the primary control(s) on mineral assemblage development in coexisting metagabbro and metabasalt is important for understanding how to interpret the geologic record of subduction processes, including interpreting evidence for fluid-rock interaction and deformation from mineral assemblages and textures.

In this paper, we focus on the Sivrihisar Massif (Turkey), in which layers of fine-grained HP/LT metabasite contain rare, coarse-grained mafic pods inferred to be metagabbro (Fig. 1). Fine- and coarse-grained metabasite both contain lawsonite and omphacite, indicating HP/LT conditions, but there are significant differences in their texturally early (prograde), peak, and texturally late (retrograde) mineral assemblages. Fine-grained Sivrihisar metabasalt has been previously studied (e.g., Davis and Whitney 2006, 2008; Çetinkaplan et al. 2008; Whitney et al. 2014; Fornash et al. 2016, 2019; Fornash and Whitney 2020), but metagabbro, has not previously been described in detail from this locality. We present new petrological and geochemical data for metagabbro and use these results to determine and compare the P–T-H_2O histories of metagabbro and associated fine-grained metabasalt. The effect of P–T conditions, deformation, protolith bulk-rock composition (including H_2O content), and grain size on metamorphic transformation is evaluated in the context of different reaction histories of metagabbro and metabasalt during subduction and exhumation. Finally, we discuss the possible implications of gabbro-eclogite transformation for the development of omphacite-rich, garnet-absent omphacitite, a rock type that has been reported in many exhumed subduction complexes (e.g., Och et al. 2003; Shi et al. 2010; Fu et al. 2012; Shigeno et al. 2012; Vitale Brovarone 2013).

Geological setting of the Sivrihisar Massif in the Tavşanlı Zone, Turkey

The Tavşanlı Zone in northwestern and north-central Turkey is one of the best exposed HP/LT belts in the world (Fig. 1a; Okay 1980, 1982, 1986). This zone, the main segment of which is 50–60 km wide and ~ 250 km long, is primarily

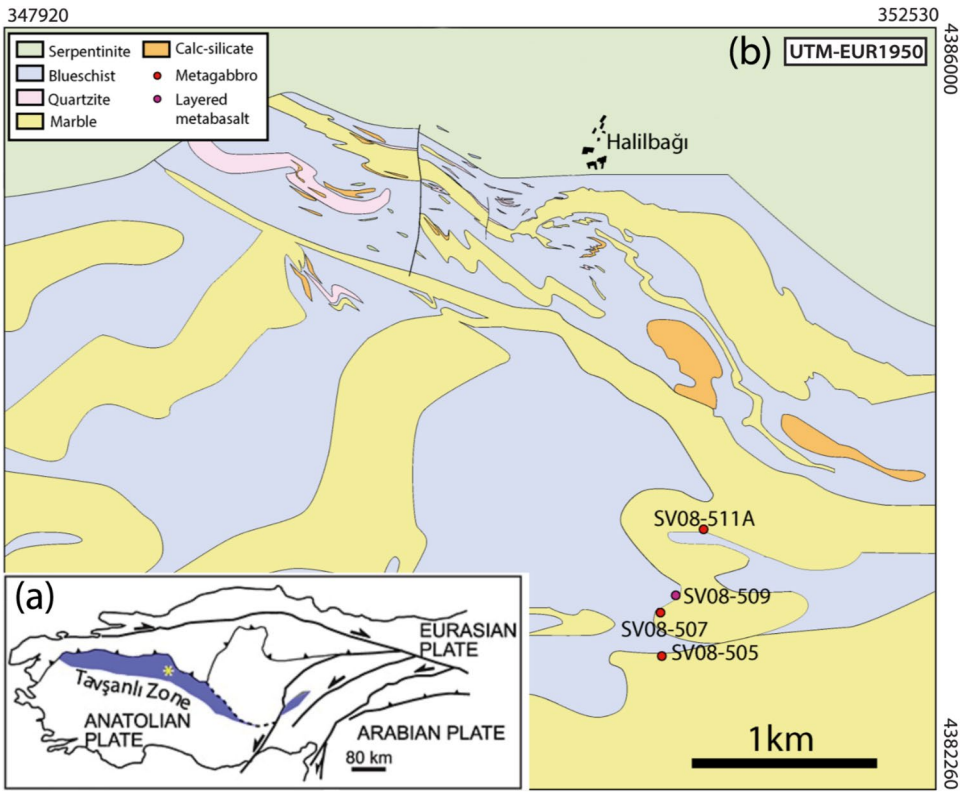

Fig. 1 **a** Simplified geologic map, showing the locations of the Tavşanlı Zone and the Sivrihisar Massif (asterisk) in Turkey (modified from Whitney et al., 2014). **b** Geologic map of the northwestern part of the Sivrihisar Massif, near the village of Halilbağı, showing the locations of samples analyzed in this study (modified from Davis and Whitney, 2006; Whitney et al., 2014)

composed of blueschist facies rocks formed by subduction of passive continental margin and Neotethyan shallow marine sequences during convergence of the Anatolide-Tauride microcontinent with Eurasia in the Late Cretaceous (Okay and Kelley 1994; Sherlock et al. 1999; Davis and Whitney 2006; Okay and Whitney 2010; Plunder et al. 2013; Fornash et al. 2016).

The Sivrihisar Massif is located at the eastern end of the main east–west segment of the Tavşanlı Zone (Fig. 1a). The massif is primarily composed of interlayered metasedimentary (marble, quartzite, calc-schist) and metabasite units (Fig. 1b). Metabasite and metasedimentary rocks both contain lawsonite, and lawsonite-bearing eclogite is locally well-preserved (Davis and Whitney, 2006; Whitney and Davis 2006). Lawsonite eclogite occurs as meter-scale elliptical pods (garnet + omphacite + lawsonite + phengite + rutile) within blueschist, quartzite, or calc-schist, and as cm-to-dm-scale layers alternating with lawsonite blueschist (glaucophane + lawsonite + phengite ± garnet ± relict omphacite ± rutile rimmed by titanite) (Kulaksız 1978; Davis and Whitney 2006, 2008; Teyssier et al. 2010; Whitney et al. 2014; Fornash et al. 2016). More rare rock types include metagabbro, serpentinite, and an omphacite + quartz + lawsonite rock interpreted as metatuff (Çetinkaplan et al. 2008; Davis and Whitney 2008; Whitney et al. 2014). Most eclogite pods and host blueschist are fine-grained and have been interpreted to have a similar basaltic protolith based on compositional and textural features (Davis and Whitney 2006). Estimated peak P–T conditions of lawsonite eclogite and some blueschist are ~ 2.4 GPa and ~ 550 °C, whereas some lawsonite blueschist records lower pressure conditions (1.5 GPa), interpreted as retrograde based on textural features and geochronology data (Davis and Whitney 2006, 2008; Whitney and Davis 2006; Mulcahy et al. 2014; Fornash et al. 2016).

In the following section, we describe the mineral assemblages, compositions, and textures of rare metagabbro from the Sivrihisar Massif, and compare these features with nearby fine-grained metabasite. We focus in particular on differences between coarse- and fine-grained metabasite, and use compositional data and phase equilibria modeling to understand these differences.

Analytical methods

Mineral analysis

Mineral compositions were determined with a JEOL 8900 Electron Microprobe in the Department of Earth Sciences at the University of Minnesota. Quantitative analyses were performed using a 20 nA beam current, a 15 kV accelerating voltage, and a focused beam for garnet and pyroxene. To prevent beam damage and Na and K loss, a defocused 5 µm beam was used for amphibole, white mica, epidote, and plagioclase. Lawsonite was analyzed with a 10 µm beam size and a 15 nA beam current. Modal amounts of minerals were determined by energy-dispersive X-ray spectroscopy (EDS) mapping analyses of selected areas within thin sections with a high resolution of 514 × 384 pixels. Mineral abbreviations are after Whitney and Evans (2010).

Whole-rock analysis

Major-element bulk-compositions were determined by X-Ray Fluorescence (XRF) at the GeoAnalytical Lab at Washington State University. To take into account the difference in grain size, a much larger representative volume was considered for the analysis of coarse-grained metagabbro relative to that of fine-grained metabasalt. Total iron content (FeO_{tot}) is reported as FeO. H_2O content was determined by loss on ignition.

Petrography and mineral compositions

Petrographic and mineral composition analyses focused on four representative samples from the northwestern part of the Sivrihisar Massif, near the village of Halilbağı (Fig. 1b): three samples of metagabbro (SV08-505, 507, 511A) from meter-scale coarse-grained pods (Figs. 2a, b) hosted by fine-grained metasedimentary rocks (marble/calc-silicate, quartzite) and/or metabasalt, and one sample of fine-grained mafic rock (inferred metabasalt; SV08-509) (Figs. 2c, d) interlayered with metasedimentary rocks. Mineral assemblages developed at various stages of metamorphic evolution (i.e., prograde, peak, and retrograde conditions), in addition to features inherited from the magmatic protolith, are summarized in Table 1 together with the grain sizes and modal abundances of major minerals. Notable features of all analyzed metagabbro are the presence of lawsonite and omphacite, and the relative scarcity of garnet. Only one metagabbro sample (SV08-507) contains glaucophane. Corona structures have not been observed in Sivrihisar metabasites.

Glaucophane-bearing metagabbro (SV08-507)

This rock, which is significantly less retrogressed than the other two metagabbro samples, occurs as a pod hosted by interlayered carbonate and quartz-rich metasedimentary layers (Fig. 1b). This metagabbro appears coarse-grained, because it contains abundant, coarse (0.2–1.8 cm), relict clinopyroxene (Figs. 3a–c). The clinopyroxene is surrounded by a matrix of fine-grained lawsonite that defines a foliation and lineation with matrix omphacite and phengite (Figs. 3a, b); this fabric is concordant with that of a

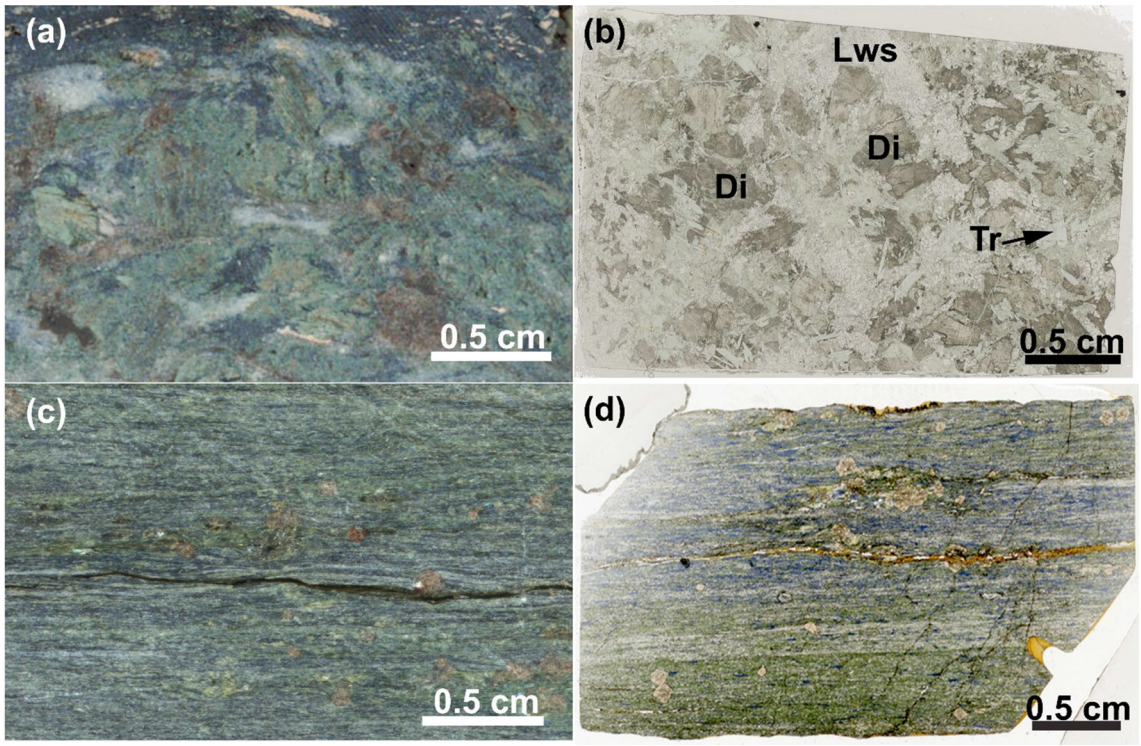

Fig. 2 Photographs of metagabbro and layered metabasalt. **a** Small polished sample of metagabbro (SV08-507). **b** Scanned thin section image of metagabbro (plane polarized light, PPL; SV08-505). **c** Small polished sample of layered metabasalt (SV08-509). **d** Scanned thin section image of metabasalt, showing alternating omphacite-rich and glaucophane-rich layers, both containing garnet and lawsonite (plane polarized light, PPL; SV08-509). Mineral abbreviations follow the recommendations of Whitney and Evans (2010)

fine-grained lawsonite + glaucophane blueschist that wraps the metagabbro pod (Figs. 3b, c). Other phases present are quartz ± titanite ± garnet, with chlorite as a texturally secondary phase.

Relict clinopyroxene has the composition of aegirine-augite to augite to diopside ($jd_{5-28}ae_{5-58}quad_{23-90}$; Quad represents Ca-Mg-Fe pyroxene) (Fig. 4, Table 2) and it has been partially boudinaged and filled with an aggregate of omphacite (Fig. 3a), which shows a wider range of compositional variation in lawsonite-rich layers ($jd_{28-39}ae_{2-26}quad_{46-60}$) than in glaucophane-rich layers ($jd_{22-32}ae_{18-24}quad_{48-59}$) (Fig. 4, Table 2). Fine-grained omphacite also occurs as inclusions within matrix garnet (Fig. 3d), and it has a range of composition ($jd_{25-34}ae_{12-23}quad_{51-55}$) consistent with fine-grained matrix omphacite in both lawsonite-rich ($jd_{21-32}ae_{14-21}quad_{51-60}$) and glaucophane-rich layers ($jd_{20-29}ae_{18-22}quad_{52-58}$) (Fig. 4, Table 2).

Garnet is a minor matrix phase in lawsonite-rich layers and exhibits a textural equilibrium with fine-grained omphacite, phengite, and lawsonite (Fig. 3d). Garnet is typically subhedral, and contains inclusions of lawsonite, omphacite, and glaucophane (Fig. 3d). Some rutile inclusions in garnet preserve rare tremolite inclusions. The composition of garnet is slightly zoned with the core higher in Ca but lower in Fe than the rim; core: $alm_{59}sps_{10}prp_{7}grs_{24}$; rim: $alm_{60}sps_{10}prp_{7}grs_{23}$ (Table 2). Subsequent minor changes in Ca, Mg, and Fe are locally present at the outermost rim ($alm_{57-59}sps_{10}prp_{6-7}grs_{24-26}$).

Matrix glaucophane is texturally late relative to both relict and metamorphic clinopyroxene. In some cases, matrix glaucophane forms a sigmoidal trail that impinges the coarse-grained relict clinopyroxene (Fig. 3c). The typical composition of matrix glaucophane has an X_{Mg} of 0.60–0.66, which is consistent in both lawsonite-rich and glaucophane-rich layers (Table 2).

Matrix lawsonite in both lawsonite-rich and glaucophane-rich layers shows a decrease in FeO_{tot} (1.51–2.60 to 0.59–1.24 wt%) and TiO_2 (0.07–0.09 to 0.02–0.05 wt%) outward from the core, followed by an increase toward the rim (FeO_{tot} = 1.27–1.51, TiO_2 = 0.04–0.30 wt%) (Table 2). Some lawsonite grains cross-cut the grain boundaries of the relict clinopyroxene (Fig. 3c). Phengite has a consistent Si abundance of ~ 3.5 p.f.u. (Table 2).

Glaucophane-free metagabbro (SV08-505, 511A)

The other two metagabbro samples (SV08-505, 511A) are from 1 to 2.5 m long pods hosted by metasedimentary rocks

Table 1 Grain sizes, modal abundances, and parageneses of minerals in metagabbro and metabasalt

Glaucophane-bearing Metagabbro (SV08-507)

	Grain Size (In length; μm)	Mode% (Lws-rich layers)	Mode% (Gln-rich layers)
Relict Cpx	2000–18000	3	5
Omp	130–500	17	12
Lws	40–280	45	27
Ph	100–300	9	8
Gln	130–750	15	30
Grt	1000	< 1	N.A.
Qz	~ 30	3	7
Rt	~ 50	<< 1	< 1
Ttn	30–260	<< 1	< 1
Chl (along crack)	100–520	7	9

Glaucophane-free Metagabbro (SV08-505, 511A)

	Grain Size (In length; μm)	Mode% (SV08-505)	Mode% (SV08-511A)
Relict Cpx	500–4000	12	12
Omp	30–200	< 2	< 2
Lws	30–12000	38	31
Ep	210–860	N.A.	17
Ph	< 10	3	3
Tr	500–5250	12	10
Ab	90–450	14	7
Ttn	40–100	< 1	< 1
Chl (along crack)	50–630	15	13
Cal (vein)	< 180	< 3	< 4

Metabasalt layers (SV08-509)

	Grain Size (In length; μm)	Mode% (BLS layers)	Mode% (ECL layers)
Omp	180–430	13	36
Lws	60–390	29	33
Ep	210–860	6	2
Ph	210–750	6	9
Gln	50–1400	41	16
Grt	330–1400	3	2
Qz	10–40	< 1	< 1
Rt	50–170	< 1	< 1
Ttn	< 10	<< 1	<< 1
Chl (along crack)	< 170	<< 1	<< 1
Ab (Grt inclusion)	10		<< 1

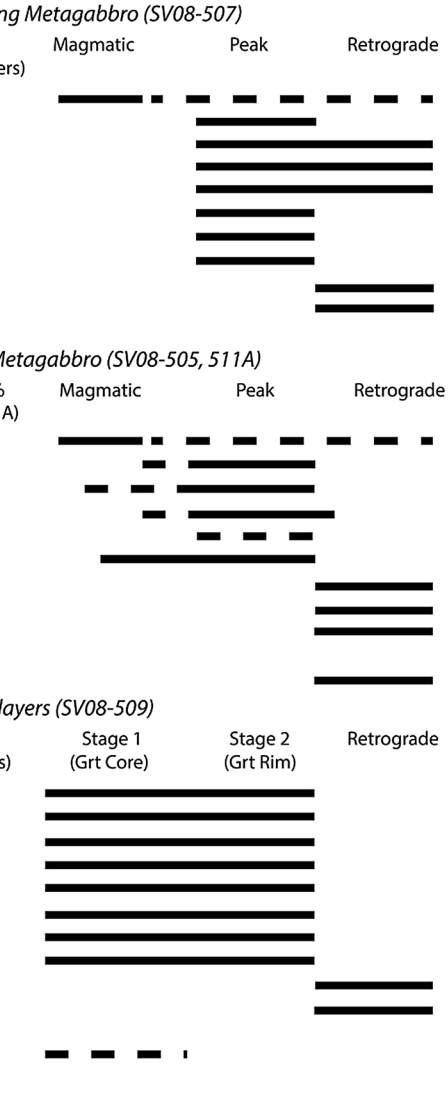

Dashed lines represent phases presumed to be stable or metastable (i.e. relict clinopyroxene) on the basis of textural evidence

(calc-schist, quartzite) that are interlayered with fine-grained metabasite (Fig. 1b). These two metagabbro samples have similar mineral assemblages, consisting of lawsonite + relict igneous clinopyroxene + metamorphic clinopyroxene + tremolite, with chlorite + titanite + calcite as texturally late phases. Albite is also present, post-dating (partially replacing) lawsonite. A K-bearing phase, likely a white mica, occurs as small irregular patches inside the matrix phases, but it is too small for an accurate compositional analysis. The major difference between these two samples is the presence of epidote in SV08-511A.

Matrix clinopyroxene is variable in grain size and composition (Table 1). Coarse-grained relict clinopyroxene has the composition of diopside, and fine-grained metamorphic clinopyroxene is compositionally zoned from aegirine-augite-rich core ($jd_{16\text{-}17}ae_{18\text{-}19}quad_{64\text{-}66}$) to omphacitic rims ($jd_{25\text{-}26}ae_{17\text{-}22}quad_{53\text{-}56}$) (Fig. 4; Table 3). Some relict diopside grains show a partial replacement by coarse-grained hydrous minerals, such as tremolite or lawsonite (Figs. 3e, f). In particular, diopside grains partially replaced by tremolite likely indicate uralitic alteration and they exhibit a slight but noticeable decrease in the quad component (0.99–0.89) and a simultaneous minor increase in the jadeite component (0–0.06) toward the rims (Table 3). Similar variations also exist in the composition of diopside that shows no textural replacement, especially at ~ 240–270 μm from the rims; core: $jd_{2\text{-}3}ae_{0\text{-}1}quad_{97\text{-}98}$, at ~ 240–270 μm from the rims: $jd_{3\text{-}5}ae_{1\text{-}2}quad_{93\text{-}97}$, rim: $jd_{1\text{-}2}ae_{0\text{-}1}quad_{97\text{-}99}$ (Table 3).

Amphibole is variable in size (Table 1). Fine-grained matrix amphibole is in textural equilibrium with fine-grained matrix omphacite and lawsonite and in some cases cross-cuts the grain boundaries of texturally earlier coarse-grained

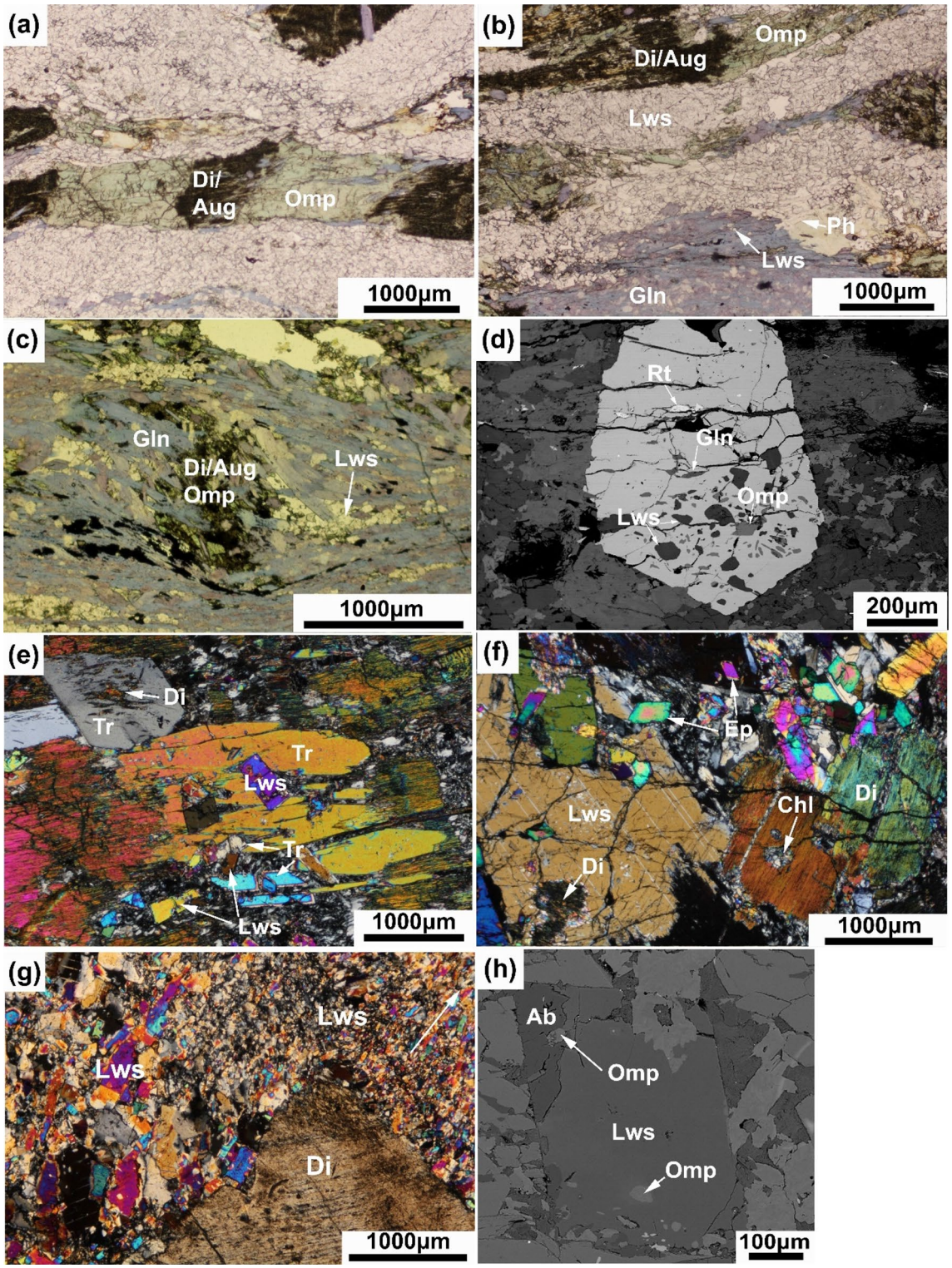

amphibole (Fig. 3e). Regardless of textural site, all amphibole in the metagabbro is tremolite. The typical composition of matrix tremolite has an X_{Mg} ($Mg^{2+}/(Mg^{2+}+Fe^{2+})$) of 0.94–0.99, decreasing slightly to 0.92 near relict diopside that is partially replaced by tremolite (Table 3).

In addition to coarse-grained lawsonite that has partially replaced relict diopside, fine-grained matrix lawsonite cross-cuts the grain boundaries of coarse-grained diopside and tremolite (Fig. 3e). In contrast, some other lawsonite grains are included in coarse-grained tremolite, suggesting they

◂**Fig. 3** Images of metagabbro. **a** Relict coarse-grained augite/diopside (dark area) boudinaged and filled by a mosaic of omphacite (green area) (PPL; SV08-507). **b** Photomicrograph showing foliation, defined by omphacite, glaucophane, lawsonite, and phengite in a lawsonite-rich matrix of a coarse-grained metagabbro pod (PPL; SV08-507). Foliation is concordant with that of lawsonite + glaucophane blueschist at the bottom. **c** Coarse-grained relict clinopyroxene impinged by sigmoidal trails of glaucophane (PPL; SV08-507). **d** BSE image (SV08-507) showing garnet with inclusions of lawsonite, omphacite, glaucophane, and rutile. **e** Relict clinopyroxene partially replaced by coarse-grained amphibole (> 1100 μm). Lawsonite occurs as inclusions in coarse-grained amphibole or cross-cuts relict clinopyroxene and coarse-grained amphibole (XPL; SV08-505). **f** Clinopyroxene partially replaced by coarse-grained matrix lawsonite (> 1200 μm) (XPL; SV08-511A). **g** Fine-grained lawsonite in contact with coarse-grained relict clinopyroxene displays a preferred orientation, which is indicated by an arrow (XPL; SV08-505). **h** BSE image (SV08-505) showing lawsonite partially replaced by albite. Both albite and lawsonite contain omphacite inclusions

formed before the host tremolite (Fig. 3e). Most fine-grained matrix lawsonite displays a shape-preferred orientation (Fig. 3g) and some grains contain omphacite and/or epidote as inclusions (Figs. 3f, h). Omphacite inclusions also occur in secondary albite that has partially replaced lawsonite (Fig. 3h). Lawsonite is slightly zoned in Fe and Ti. From core to rim, Fe increases and Ti decreases; core: 0.56–1.18, rim: 0.80–1.70 wt% FeO_{tot}; core: 0.12–0.22, rim: < 0.11 wt% TiO_2 (Table 3). A few lawsonite grains in the epidote-bearing metagabbro (SV08-511A) exhibit a subsequent increase in Ti (to 0.12–0.16 wt% TiO_2) within ~ 240 μm of the rim.

Epidote is present as a matrix phase with variable grain size (Table 1) in one metagabbro (SV08-511A) and appears to be texturally late relative to lawsonite (e.g., it impinges the grain boundaries of coarse-grained lawsonite; Fig. 3f). Some epidote grains appear to be included in coarse-grained lawsonite (Fig. 3f) and are slightly less Fe^{3+}-rich (e.g., $Fe^{3+}/(Fe^{3+} + Al) = 0.19–0.21$) compared to matrix epidote (e.g., 0.20–0.22) (Table 3).

Although the samples lack garnet, the presence of lawsonite and omphacite in the matrix and omphacite inclusions in lawsonite (Fig. 3h) indicate HP/LT conditions during subduction metamorphism.

Fine-grained metabasite layers (SV08-509)

Within 300 m of the sampled metagabbro pods, a sample (SV08-509) was collected from fine-grained, garnet-bearing metabasite that is interlayered with metasedimentary rocks (dominantly marble; Fig. 1b). Although fine-grained Sivrihisar metabasite has been well described in previous work (Davis and Whitney 2006), we include a detailed summary of this sample for comparison with the nearby metagabbro. The fine-grained metabasite comprises thin glaucophane-rich and omphacite-rich layers, alternating at the millimeter to centimeter-scale (Figs. 2c, d). All layers contain lawsonite + glaucophane + omphacite + phengite + garnet + epidote ± quartz ± rutile, but vary in the modal amounts of glaucophane and omphacite (Fig. 2d, Table 1). Fine-grained matrix omphacite, lawsonite, phengite, and glaucophane define a strong foliation and lineation (Figs. 2d, 5a).

Garnet porphyroblasts are euhedral and variable in size (Table 1) in both eclogite (omphacite-rich) and blueschist (glaucophane-rich) layers. Large garnets contain inclusions of lawsonite, glaucophane, omphacite, epidote, quartz, rutile, and albite (Fig. 5b). Small garnets contain few inclusions; rutile is the most common inclusion phase. Large garnets have similar compositions in blueschist and eclogite layers, with cores significantly higher in Mn, slightly higher in Ca, significantly lower in Fe, and slightly lower in Mg relative to rims; core: $alm_{56-57}sps_{14-15}prp_5grs_{24-25}$, rim: $alm_{64-65}sps_{5-6}prp_{7-8}grs_{22-23}$ (Fig. 6, Table 4). This is similar to the garnet compositions reported for lawsonite blueschist in the same region (Davis and Whitney 2006). Subsequent increase in Mn and Ca and decrease in Mg and Fe is locally present at the outermost rims ($alm_{61}sps_{7-10}prp_{6-7}grs_{23-25}$). Small garnets are only slightly zoned, with compositions of both core and rim similar to the rims of large garnets (Table 4).

Only minor zoning is observed in fine-grained omphacite. From core to rims, fine-grained omphacite in eclogite layers is characterized by decreasing and then increasing jadeite component (core: 0.26–0.28, mantle: 0.23–0.24, rim: 0.26–0.28) (Fig. 4, Table 4). Systematic variation is also present in the aegirine component, which increases and then decreases toward the rims (core: 0.28–0.32, mantle: 0.31–0.36, rim: 0.28–0.31) (Fig. 4, Table 4). The quad component also changes but without systematic variation (0.40–0.46) (Fig. 4, Table 4). In blueschist layers, fine-grained omphacite shows slight variations in the jadeite (0.19–0.22 to 0.26–0.29), aegirine (0.25–0.28 to 0.24–0.26), and quad components (0.53 to 0.45–0.50) toward the rims (Fig. 4, Table 4).

The composition and zoning of omphacite inclusions vary slightly depending on whether the host garnet is in an eclogite or blueschist layer. For garnet in eclogite layers, omphacite inclusions show a slight decrease in the jadeite component (0.26 to 0.22–0.24) and an increase in the quad component (0.42–0.47 to 0.48–0.51) with a minor change in the aegirine component (0.27–0.32) (Fig. 4, Table 4). If the host garnet is in blueschist layers, omphacite inclusions increase slightly in the jadeite component (0.22–0.24 to 0.28) and decrease in the aegirine (0.25–0.29 to 0.22–0.27) and quad components (0.49–0.51 to 0.45–0.50) from core to rims (Fig. 4, Table 4).

Lawsonite, glaucophane, and phengite in the matrix are variable in grain size (Table 1) and their compositions are consistent in both eclogite and blueschist layers. Matrix lawsonite shows a slight increase in FeO_{tot} (1.55–1.87 to

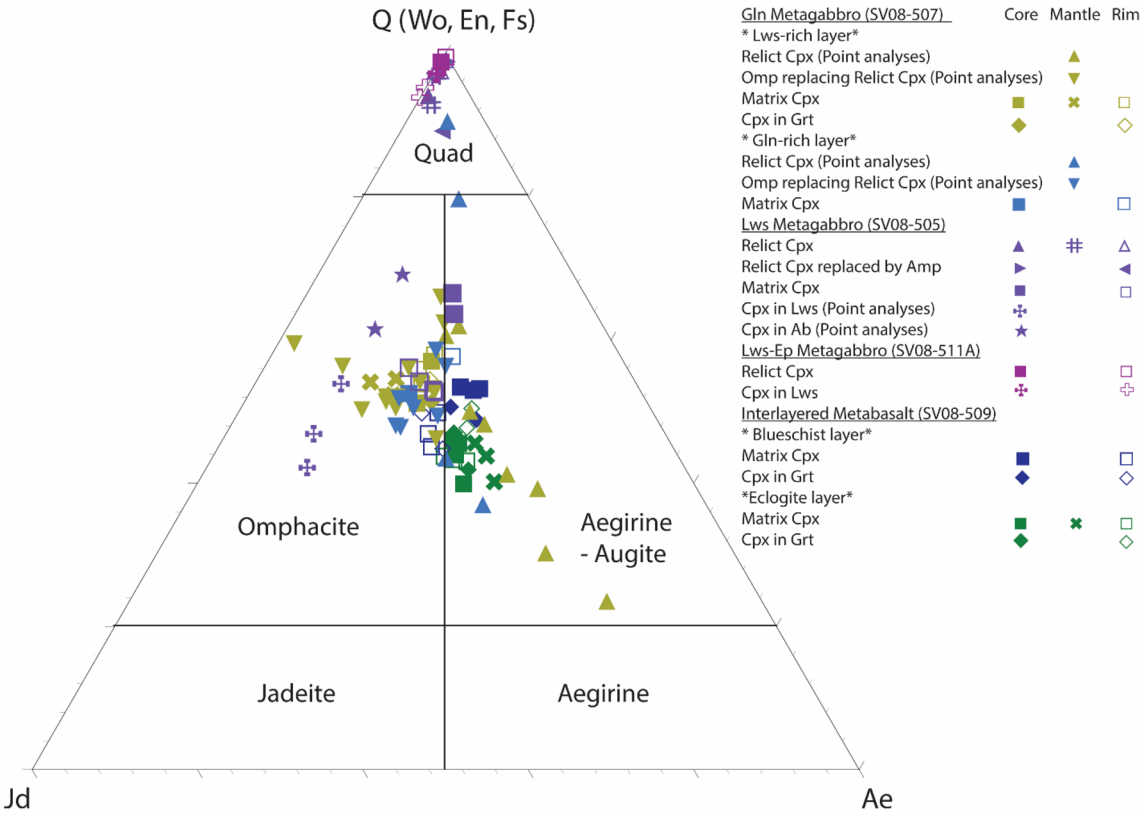

Fig. 4 Compositional diagram of clinopyroxene in metagabbro and metabasalt. Core and rim compositions are plotted. Compositions of locations between core and rim (called 'mantle') are also plotted for the grain that exhibits complex compositional zoning. Individual analyses for omphacite inclusions (< 40 μm long) in albite and lawsonite in metagabbro are also plotted

1.66–1.89 wt%) and TiO_2 (0.07–0.12 to 0.10–0.16 wt%) toward the rim (Table 4). Glaucophane and phengite have a consistent range of X_{Mg} (0.63–0.72) (Table 4) and Si (3.43–3.53 p.f.u.), respectively.

Matrix epidote has a variable grain size (Table 1). Glaucophane and omphacite are common inclusions in large epidote, whereas fine-grained epidote is inclusion-free. Epidote inclusions in garnet are slightly lower in pistacite content ($Fe^{3+}/(Fe^{3+}+Al)=0.26–0.28$) compared to matrix epidote (0.29–0.33), and both are similar to previous compositions reported for epidote in blueschist (0.3–0.31) and eclogite (0.23–0.36) from this region (Davis and Whitney 2008) (Table 4).

Bulk rock compositions

The bulk compositions of the glaucophane-bearing metagabbro (SV08-507), the glaucophane-free metagabbro (SV08-505), and the fine-grained metabasalt (SV08-509) were determined in order to compare them and to construct phase diagrams (pseudosections) for modeling the P–T-H_2O conditions of prograde mineral assemblages. The possible compositional heterogeneity (including H_2O) of protoliths was investigated to assess its influence on metamorphic mineral assemblage.

Major element compositions

The bulk-rock major element compositions of the two glaucophane-absent metagabbro samples (SV08-505, 511A) analyzed in this study are generally low in FeO_{tot} (4.26–4.84 wt%), TiO_2 (0.24–0.32 wt%), K_2O (0.03–0.06 wt%), P_2O_5 (< 0.02 wt%) and Na_2O (0.30–1.66 wt%), and have relatively high MgO (10.56–10.60 wt%) and CaO (15.52–17.15 wt%) contents (Table 5). Compared to these metagabbro samples, the fine-grained metabasalt sample (SV08-509) and the glaucophane-bearing metagabbro (SV08-507) analyzed in this study have significantly lower MgO (5.08–6.39 wt%) and CaO (9.17–10.63 wt%) and higher FeO_{tot} (8.61–10.45 wt%), TiO_2 (1.07–1.37 wt%), K_2O (0.61–1.25 wt%), P_2O_5 (0.02–0.10) and Na_2O (3.78–3.79 wt%) (Table 5).

Table 2 Representative compositions of clinopyroxene, garnet, amphibole, lawsonite, and phengite in glaucophane-bearing metagabbro

	Glaucophane-bearing Metagabbro (SV08-507)								
	Omp in Grt (Lws-rich layers)	Relict Cpx (Lws-rich layers)	Omp replacing Relict Cpx (Lws-rich layers)	Matrix Omp (Lws-rich layers)	Omp replacing Relict Cpx (Gln-rich layers)	Matrix Omp (Gln-rich layers)		Grt Core (Lws-rich layers)	Grt Rim (Lws-rich layers)
SiO_2	54.79	53.87	55.13	55.17	53.75	54.13	SiO_2	37.58	37.34
TiO_2	0.05	0.25	0.07	0.03	0.13	< d.l	TiO_2	0.10	0.04
Al_2O_3	6.31	5.33	7.63	6.46	6.42	6.87	Al_2O_3	20.38	20.81
Cr_2O_3	< d.l	0.06	< d.l	< d.l	< d.l	< d.l	Cr_2O_3	< d.l	0.04
FeO_{tot}	11.44	13.85	10.45	11.16	11.54	10.82	FeO_{tot}	27.39	27.94
MnO	0.18	0.14	0.11	0.09	0.27	0.08	MnO	4.38	4.22
MgO	7.36	7.58	6.78	7.14	7.18	7.40	MgO	1.69	1.78
CaO	13.05	11.33	11.72	12.93	12.18	12.87	CaO	8.54	8.05
Na_2O	6.86	7.21	7.07	6.95	7.02	6.63	Na_2O	0.04	< d.l
K_2O	< d.l	< d.l	0.03	< d.l	< d.l	< d.l	K_2O	< d.l	< d.l
Total	100.04	99.62	98.99	99.93	98.49	98.8	Total	100.1	100.22
Equiv. O	6	6	6	6	6	6	Equiv. O	12	12
Si	2.03	2.02	2.04	2.04	2.02	2.02	Si	3.01	2.99
Ti	0.00	0.01	0.00	0.00	0.00	0.00	Ti	0.01	0.00
Al	0.28	0.24	0.33	0.28	0.28	0.30	Al	1.93	1.96
Cr	0.00	0.00	0.00	0.00	0.00	0.00	Cr	0.00	0.00
Fe	0.35	0.44	0.32	0.34	0.36	0.34	Fe	1.84	1.87
Mn	0.01	0.00	0.00	0.00	0.01	0.00	Mn	0.30	0.29
Mg	0.41	0.42	0.37	0.39	0.40	0.41	Mg	0.20	0.21
Ca	0.52	0.46	0.46	0.51	0.49	0.51	Ca	0.73	0.69
Na	0.49	0.53	0.51	0.50	0.51	0.48			
							Sps	0.10	0.10
Jd	0.26	0.21	0.35	0.28	0.26	0.28	Pyp	0.07	0.07
Ae	0.23	0.31	0.15	0.21	0.24	0.19	Alm	0.59	0.60
Quad	0.51	0.48	0.50	0.51	0.49	0.52	Grs	0.24	0.23
	Gln (Lws-rich layers)	Gln (Gln-rich layers)		Lws Core (Lws-rich layers)	Lws Rim (Lws-rich layers)	Lws Outermost Rim (Lws-rich layers)		Ph (Lws-rich layers)	Ph (Gln-rich layers)
SiO_2	56.26	55.75	SiO_2	38.27	39.65	38.36	SiO_2	51.43	50.51
TiO_2	0.05	< d.l	TiO_2	0.07	0.04	0.12	TiO_2	0.21	0.26
Al_2O_3	9.60	8.00	Al_2O_3	30.21	32.44	31.38	Al_2O_3	23.19	23.03
Cr_2O_3	< d.l	0.06	Cr_2O_3	< d.l	< d.l	< d.l	Cr_2O_3	< d.l	< d.l
FeO_{tot}	12.15	13.31	FeO_{tot}	2.59	1.04	1.28	FeO_{tot}	4.21	4.11
MnO	0.07	0.04	MnO	< d.l	< d.l	< d.l	MnO	< d.l	< d.l
MgO	9.64	10.3	MgO	< d.l	< d.l	< d.l	MgO	4.43	4.18
CaO	0.45	1.28	CaO	17.73	17.59	17.84	CaO	0.04	0.10
Na_2O	8.26	7.77	Na_2O	< d.l	< d.l	< d.l	Na_2O	< d.l	0.19
K_2O	< d.l	0.02	K_2O	< d.l	< d.l	< d.l	K_2O	11.03	10.58
Total	96.49	96.53	Total	88.87	90.76	88.98	Total	94.54	92.97
Equiv. O/Cation	23/13	23/13	Equiv. O	8	8	8	Equiv. O	11	11
Si	7.93	7.90	Si	2.01	2.02	2.00	Si	3.51	3.48
Ti	0.01	0.00	Ti	0.00	0.00	0.00	Ti	0.01	0.01
Al	1.60	1.34	Al	1.87	1.95	1.93	Al	1.86	1.87
Fe	1.44	1.57	Fe^{3+}	0.11	0.04	0.06	Fe	0.24	0.24

Table 2 (continued)

	Gln (Lws-rich layers)	Gln (Gln-rich layers)		Lws Core (Lws-rich layers)	Lws Rim (Lws-rich layers)	Lws Outermost Rim (Lws-rich layers)		Ph (Lws-rich layers)	Ph (Gln-rich layers)
Mn	0.01	0.01	Ca	1.00	0.96	1.00	Mn	0.00	0.00
Mg	2.03	2.18					Mg	0.45	0.43
Ca	0.07	0.19					Ca	0.00	0.01
Na	2.26	2.14					Na	0.00	0.03
K	0.00	0.00					K	0.96	0.93
Mg#	0.61	0.64							
Fe^{3+}#	0.08	0.21							

FeO_{tot} = All iron is reported as FeO wt%; < d.l. = less than detection limit (i.e., analyzed but not detected); Mg# = Mg/(Mg + Fe^{2+}); Fe^{3+}# = Fe^{3+}/(Fe^{3+} + Al^{vi}); Charge balance indicates presence of little to no Fe^{2+} in lawsonite

Estimation of H_2O in the bulk-rock compositions

The bulk H_2O content was calculated from the compositions and modes of hydrous phases that appear to be in textural equilibrium (Table 5): (1) lawsonite + phengite (SV08-507); (2) lawsonite + tremolite (SV08-505); and (3) lawsonite + phengite + glaucophane + epidote (SV08-509). We assumed that the amount of H_2O retained within each hydrous phase was equal to a difference between 100% (anhydrous) and the measured total oxide weight percentages (i.e., 100 wt%—total oxide wt% measured from electron microprobe analysis). The calculated H_2O contents are compared with the measured loss-on-ignition (LOI) values in the XRF whole-rock analyses and with amounts modelled from pseudosections (Table 5). The calculated range of bulk H_2O content (5.5–9.5 wt%) is relatively higher than the range of LOI (4.8–6.8 wt%), and both calculated and measured bulk H_2O contents are higher in the metagabbro samples than in the metabasalt (Table 5). These higher values are consistent with the higher modal abundance of lawsonite (~ 30–45%) and other hydrous phases in the metagabbro samples compared to the metabasalt (Table 1).

Effective bulk-rock compositions

The composition relevant to modeling prograde P–T conditions may not be the same as the measured bulk-rock composition of a sample; e.g., as a result of the presence of relict phases, element sequestration into the cores of growing porphyroblasts, or the addition of elements during retrograde metamorphism. For that reason, the effective bulk composition (EBC) was calculated to take into account the effect of element fractionation on the analyzed metagabbro and metabasalt given the presence of relict igneous clinopyroxene (e.g., diopside and augite) and zoned garnet porphyroblasts.

Because the metabasalt (SV08-509) consists of blueschist and eclogite layers, we calculated an EBC for each layer (Evans 2004; Gaidies et al. 2006). This method applies a Rayleigh fractionation mechanism to relate the Mn content of garnet porphyroblasts to the modal proportion of garnet, and thus derives curvilinear relationships between the modal amount vs. the CaO, MgO, FeO_{tot} and MnO contents of garnet. These relationships were then used to estimate the amounts of elements fractionated into garnet relative to bulk rock composition at each stage of garnet growth. Consequently, the core composition of garnet is the most enriched in MnO owing to the progressive depletion of Mn with increasing garnet modal abundance. One of the calculated EBCs represents an equilibrium with the rim compositions of inclusion phases within garnet (Table 5; referred to as Stage 1). EBC was calculated from an initial bulk composition by subtracting the element contents sequestered up to the extent of the volume of host garnet, where the analyzed inclusion phase (i.e., omphacite) is located (Fig. 6b). The other EBC represents an equilibrium at the growth of garnet rims with the lowest Mn content, which correlates to the maximum modal % of garnet (Table 5; referred to as Stage 2). We assumed garnet rims were in equilibrium with rims of matrix minerals. The initial bulk composition of each layer was calculated based on the mineral modes and compositions of matrix phases (lawsonite + glaucophane + omphacite + phengite + garnet + epidote + quartz + rutile).

The composition of garnet in the glaucophane-bearing metagabbro (SV08-507) varies slightly from core to rim (Table 2). Thus, the composition of the garnet core was subtracted from an initial EBC (Stage 1) to account for elements sequestered during the growth of garnet. This EBC represents an equilibrium between garnet rims and other metamorphic matrix minerals (Stage 2). The initial EBC was estimated from the modes and compositions of garnet (core), omphacite, lawsonite, glaucophane, phengite, and quartz. We subtracted the chemical contribution of relict igneous clinopyroxene to construct phase diagrams that only consider metamorphic minerals.

Table 3 Representative compositions of clinopyroxene, amphibole, lawsonite, and epidote in glaucophane-free metagabbro

Glaucophane-free Metagabbro (SV08-505, 511A)																
	Relict Cpx			Relict Cpx replaced by Amp		Omp			Tr	Tr, replacing Relict Cpx		Lws			Ep	Ep included in Lws
	Core	~240 µm of the rims	Rim	Core	Rim	Core	Rim					Core	Rim			
SiO_2	52.82	52.50	53.31	54.19	54.35	54.75	55.25	SiO_2	57.11	56.32	SiO_2	37.66	37.44	SiO_2	37.58	38.19
TiO_2	0.30	0.36	0.11	0.12	0.23	< d.l	0.05	TiO_2	0.03	0.03	TiO_2	0.22	0.08	TiO_2	0.09	0.06
Al_2O_3	1.65	2.70	0.69	0.56	1.74	4.88	7.08	Al_2O_3	0.99	1.38	Al_2O_3	30.89	30.76	Al_2O_3	24.53	25.43
Cr_2O_3	0.18	0.16	0.11	0.11	0.09	< d.l	< d.l	Cr_2O_3	0.04	< d.l	Cr_2O_3	0.08	0.04	Cr_2O_3	0.08	0.07
FeO_{tot}	4.77	5.67	4.33	4.18	5.71	5.60	5.89	FeO_{tot}	5.12	5.49	FeO_{tot}	0.62	0.88	FeO_{tot}	9.72	8.70
MnO	0.17	0.15	0.15	0.14	0.22	0.13	0.14	MnO	0.14	0.17	MnO	< d.l	0.04	MnO	0.06	0.09
MgO	15.43	14.92	16.02	16.70	14.71	11.43	9.73	MgO	21.78	20.66	MgO	0.01	0.02	MgO	0.03	0.05
CaO	23.60	21.47	24.15	24.42	21.84	17.51	14.85	CaO	11.99	12.05	CaO	17.89	17.75	CaO	23.44	23.41
Na_2O	0.31	0.99	0.14	0.18	1.53	5.31	7.04	Na_2O	0.66	0.88	Na_2O	< d.l	< d.l	Na_2O	< d.l	< d.l
K_2O	< d.l	< d.l	< d.l	< d.l	< d.l	< d.l	< d.l	K_2O	0.12	0.12	K_2O	< d.l	0.01	K_2O	< d.l	< d.l
Total	99.22	98.92	99.00	100.60	100.44	99.60	100.03	Total	97.98	97.11	Total	87.36	87.02	Total	95.55	96.01
Equiv.O	6	6	6	6	6	6	6	Equiv.O/Cation	23/13	23/13	Equiv.O	8	8	Equiv O	12.5	12.5
Si	1.96	1.95	1.98	1.98	1.99	2.00	2.00	Si	7.80	7.83	Si	2.01	2.00	Si	3.09	3.10
Ti	0.01	0.01	0.00	0.00	0.01	0.00	0.00	Ti	0.00	0.00	Ti	0.01	0.00	Ti	0.01	0.00
Al	0.07	0.12	0.03	0.02	0.08	0.21	0.30	Al	0.16	0.22	Al	1.94	1.94	Al	2.38	2.43
Cr	0.00	0.00	0.00	0.00	0.00	0.00	0.00	Fe	0.59	0.64	Fe^{3+}	0.02	0.03	Cr	0.01	0.00
Fe	0.15	0.18	0.13	0.13	0.17	0.17	0.18	Mn	0.02	0.02	Ca	1.02	1.02	Fe	0.67	0.59
Mn	0.01	0.00	0.00	0.00	0.01	0.00	0.00	Mg	4.43	4.28				Mn	0.00	0.01
Mg	0.85	0.83	0.89	0.91	0.80	0.62	0.53	Ca	1.75	1.79				Mg	0.00	0.01
Ca	0.94	0.85	0.96	0.95	0.86	0.69	0.58	Na	0.18	0.24				Ca	2.06	2.04
Na	0.02	0.07	0.01	0.01	0.11	0.38	0.50	K	0.02	0.02						
Jd	0.02	0.05	0.01	0.00	0.06	0.17	0.25									
Ae	0.01	0.02	0.00	0.01	0.05	0.19	0.22	Mg#	0.99	0.92						
Quad	0.97	0.93	0.99	0.99	0.89	0.64	0.53	Fe^{3+}#	1.00	0.83				$Fe^{3+}/(Fe^{3+}+Al)$	0.22	0.19

FeO_{tot} = All iron is reported as FeO wt%; < d.l. = less than detection limit (i.e., analyzed but not detected); Mg# = $Mg/(Mg+Fe^{2+})$; Fe^{3+}# = $Fe^{3+}/(Fe^{3+}+Al^{vi})$; Charge balance indicates presence of little to no Fe^{2+} in lawsonite; Ps = Pistacite content ($Fe^{3+}/(Fe^{3+}+Al)$)

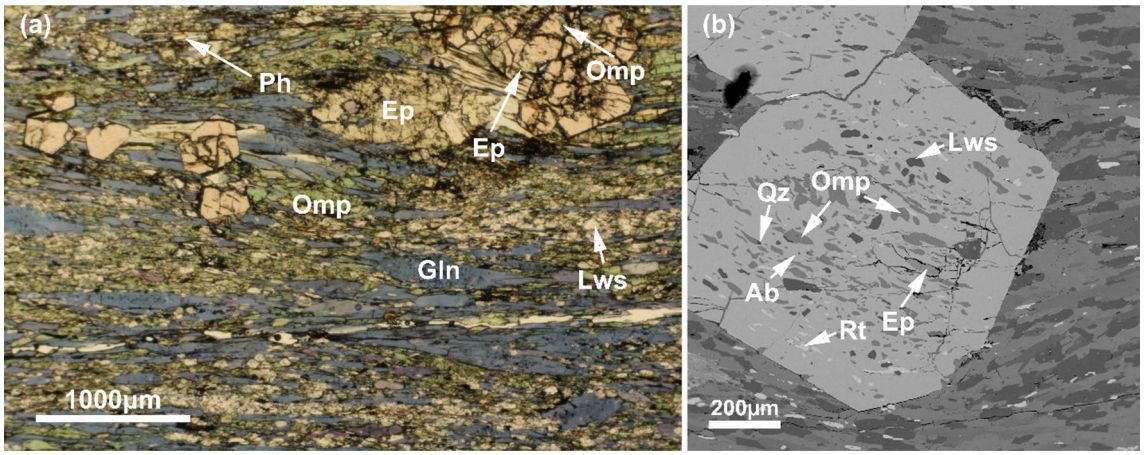

Fig. 5 Images of the fine-grained, layered metabasalt (SV08-509). **a** Photomicrograph showing glaucophane-rich and omphacite-rich domains (PPL; SV08-509). Foliation is defined by omphacite, glaucophane, phengite, and lawsonite. Note the coarse epidote and the garnet porphyroblast with inclusions of omphacite and epidote. **b** BSE image (SV08-509) of large garnet with inclusions of lawsonite, omphacite, epidote, quartz, rutile, and plagioclase

The compositional effects of element-sequestration and -introduction into the glaucophane-free metagabbro (SV08-505) were accounted for by subtracting the compositional contribution of relict igneous diopside and late calcite vein. Therefore, the EBC was determined from the modes and compositions of fine-grained matrix minerals (lawsonite + omphacite + tremolite) that likely attained a textural equilibrium during eclogite-facies metamorphism.

Estimation of Fe_2O_3 in the bulk-rock compositions

In metagabbro and metabasalt, compositional zoning of Fe^{3+} content as determined from calculated mineral stoichiometry occurs in clinopyroxene and/or epidote, suggesting continuous changes in the bulk mole fraction of $Fe_2O_3/(FeO + Fe_2O_3)$ (referred to as $X(Fe_2O_3)$) during growth of these minerals. Thus, it is critical to determine the $X(Fe_2O_3)$ ratio in each EBC to obtain more accurate estimates of P–T-H_2O conditions at the relevant stage of metamorphic evolution. To estimate Fe_2O_3 content, we created a series of pseudosections for each EBC by adjusting the $X(Fe_2O_3)$ of EBC from 0.1 to 0.3. In this way, we determined the appropriate range of values that can generate the best fit between measured mineral compositions and modelled compositional isopleths (Groppo and Castelli 2010). In detail, if the modelled compositional isopleths of garnet and omphacite intersect in a field in the pseudosection, and the predicted mineral assemblage is consistent with textural evidence (e.g., mineral inclusion assemblages in garnet porphyroblast), we consider that the value of $X(Fe_2O_3)$ used in the pseudosection is reasonable.

Pseudosection modeling

Phase diagrams were calculated based on the Na_2O-K_2O-CaO-MgO-FeO-Fe_2O_3-MnO-Al_2O_3-SiO_2-TiO_2-H_2O system using the Perple_X software package (Connolly 1990), the thermodynamic dataset of (Holland and Powell 1998) (updated 2011), and the following solution models: Gt(HP) for garnet (Holland and Powell 1998), Pheng(HP) for white mica (Holland and Powell 1998), Chl(HP) for chlorite (Holland et al. 1998), Ep(HP) for clinozoisite-epidote (Holland and Powell 1998), cAmph(G) for amphibole (Green et al. 2016) and Omph(GHP) for clinopyroxene (Green et al. 2007). P_2O_5 was ignored in the composition system, because P is present only in trace amounts in major silicate phases, and the primary P-bearing phase of apatite occurs as an accessory mineral. H_2O was considered to be in excess given the high modal abundance of hydrous minerals (i.e., lawsonite, amphibole, epidote, and phengite).

P–T-H_2O conditions of glaucophane-bearing metagabbro (SV08-507)

In phase diagrams constructed for pre–peak metamorphism relevant to the initiation of garnet growth (Stage 1), isopleths for X_{grs}, X_{prp}, X_{alm}, and X_{sps} corresponding to garnet core composition were contoured and determined to intersect at $X(Fe_2O_3) = 0.2$ (Online Resource 1). The predicted mineral assemblage (Ph + Grt + Gln + Omp + Lws + Rt + Qz) reasonably matches with the inclusion assemblage of

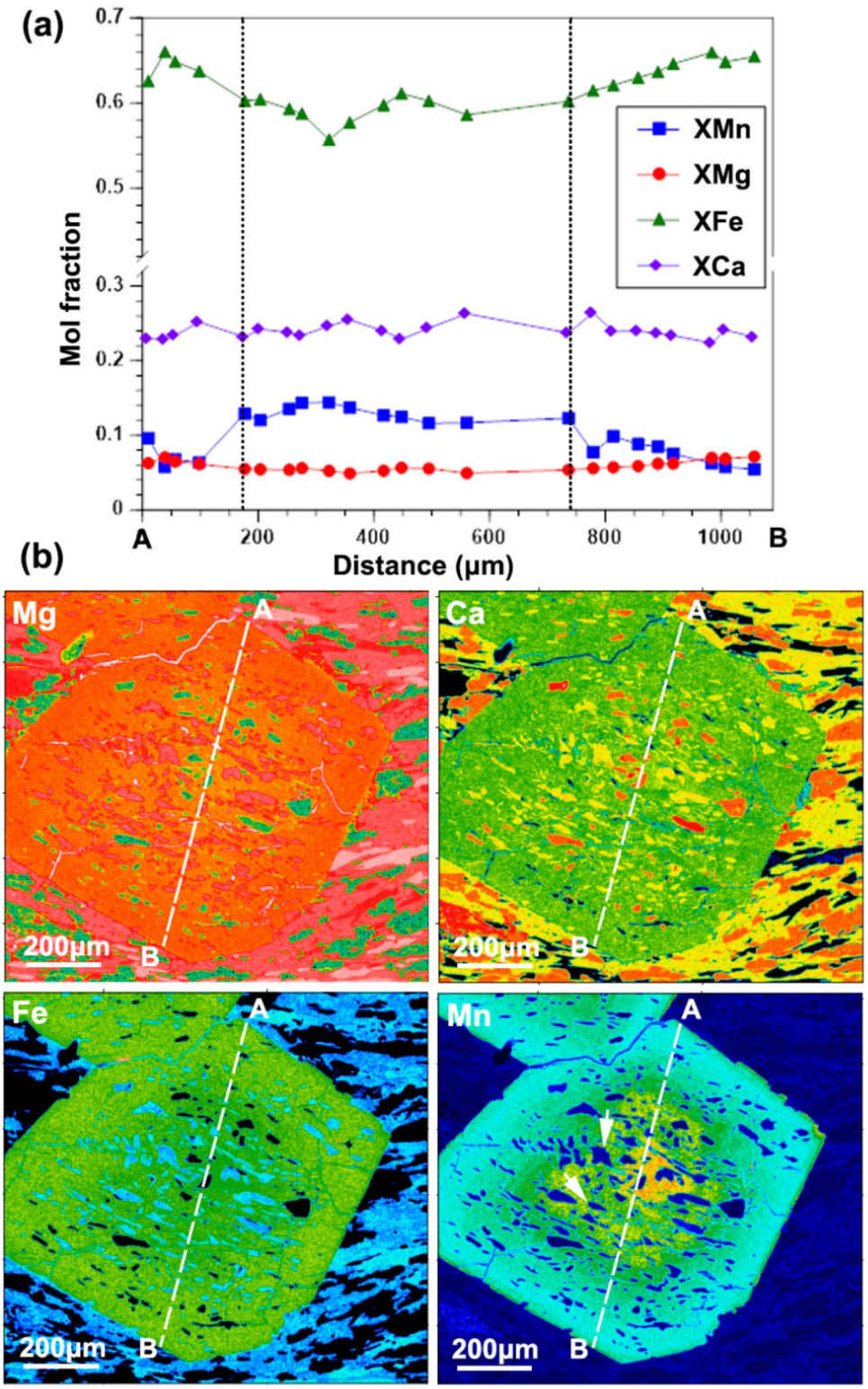

Fig. 6 **a** Compositional profiles across a representative garnet in eclogite layers of the fine-grained, layered metabasalt. Dashed lines indicate the compositions of garnet at the location of two omphacite inclusions analyzed in the study. **b** X-ray maps of element distribution in the garnet. Analytical traverses are indicated by white dashed lines. Analyzed omphacite inclusions are indicated by white arrows

garnet and it is stable at 490–500 °C and ~ 2.5 GPa with 6.4–6.6 H_2O wt% (Fig. 7a). To model the P–T-H_2O conditions at the later metamorphic stage (Stage 2), phase diagrams were contoured with the compositional isopleths corresponding to the rims of garnet and matrix omphacite. The contoured isopleths define two different regions of intersection at $X(Fe_2O_3) = 0.3$ (Fig. 7b). The compositional isopleths of garnet (X_{grs}, X_{prp}, X_{alm}, and X_{sps}) show the best intersection in the stability field of Ph + Grt + Gln + Omp + Lws + Rt + Qz at ~ 500 °C and ~ 2.5 GPa with the

Table 4 Representative compositions of clinopyroxene, garnet, amphibole, lawsonite, phengite, and epidote in metabasalt layers

	Metabasalt layers (SV08-509)												
	Omp (BLS)		Omp (ECL)			Omp in Grt (BLS)		Omp in Grt (ECL)			Large Grt		Small Grt
	Core	Rim	Core	Mantle	Rim	Core	Rim	Core	Rim		Core	Rim	
SiO_2	52.59	53.52	53.52	53.35	53.83	53.12	54.05	53.81	53.15	SiO_2	36.28	37.32	36.99
TiO_2	< d.l	< d.l	0.06	0.03	0.04	0.04	0.03	< d.l	0.06	TiO_2	0.13	0.06	0.05
Al_2O_3	5.05	6.96	6.68	5.78	6.81	5.27	6.63	6.25	5.89	Al_2O_3	19.79	20.47	20.78
Cr_2O_3	< d.l	< d.l	0.03	0.06	0.03	< d.l	0.04	0.07	< d.l	Cr_2O_3	0.04	0.13	< d.l
FeO_{tot}	13.47	13.05	14.29	13.68	12.77	13.38	13.40	13.68	14.09	FeO_{tot}	27.45	30.45	29.37
MnO	0.18	0.10	0.18	0.20	0.04	0.20	0.24	0.25	0.26	MnO	6.29	2.47	2.89
MgO	7.00	5.84	5.34	6.22	6.06	6.58	5.81	6.34	6.42	MgO	1.24	1.76	1.70
CaO	13.02	10.85	9.78	11.57	11.01	12.36	11.05	11.41	11.59	CaO	7.98	8.09	8.19
Na_2O	6.36	7.58	8.28	7.46	7.81	6.98	7.66	7.32	7.13	Na_2O	0.01	< d.l	< d.l
K_2O	< d.l	< d.l	< d.l	< d.l	< d.l	< d.l	< d.l	< d.l	< d.l	K_2O	0.01	< d.l	< d.l
Total	97.67	97.91	98.15	98.35	98.39	97.94	98.91	99.13	98.59	Total	99.22	100.74	99.99
Equiv. O	6	6	6	6	6	6	6	6	6	Equiv. O	12	12	12
Si	2.02	2.03	2.04	2.04	2.03	2.03	2.04	2.03	2.02	Si	2.97	2.99	2.98
Ti	0.00	0.00	0.00	0.00	0.00	0.00	0.00	0.00	0.00	Ti	0.01	0.00	0.00
Al	0.23	0.31	0.30	0.27	0.26	0.24	0.29	0.28	0.26	Al	1.91	1.93	1.97
Cr	0.00	0.00	0.00	0.00	0.00	0.00	0.00	0.00	0.00	Cr	0.00	0.00	0.00
Fe	0.43	0.41	0.46	0.48	0.44	0.43	0.42	0.43	0.45	Fe	1.88	2.04	1.98
Mn	0.01	0.00	0.01	0.01	0.01	0.01	0.01	0.01	0.01	Mn	0.44	0.17	0.20
Mg	0.40	0.33	0.30	0.31	0.35	0.38	0.33	0.36	0.36	Mg	0.15	0.21	0.20
Ca	0.54	0.44	0.40	0.42	0.47	0.51	0.45	0.46	0.47	Ca	0.70	0.69	0.71
Na	0.47	0.56	0.61	0.61	0.55	0.52	0.56	0.54	0.53				
										Sps	0.15	0.06	0.07
Jd	0.20	0.29	0.28	0.24	0.28	0.22	0.28	0.26	0.24	Pyp	0.05	0.07	0.07
Ae	0.27	0.26	0.32	0.31	0.28	0.29	0.27	0.27	0.29	Alm	0.57	0.64	0.63
Quad	0.53	0.45	0.40	0.46	0.44	0.49	0.45	0.47	0.48	Grs	0.24	0.23	0.24

	Gln		Lws Core		Lws Rim		Ph		Ep	Ep in Grt
SiO_2	55.49	SiO_2	37.69		37.78	SiO_2	51.33	SiO_2	36.11	37.37
TiO_2	0.06	TiO_2	0.07		0.16	TiO_2	0.18	TiO_2	0.12	0.06
Al_2O_3	6.69	Al_2O_3	31.37		31.01	Al_2O_3	23.13	Al_2O_3	21.85	23.84
Cr_2O_3	< d.l	Cr_2O_3	0.07		0.09	Cr_2O_3	0.11	Cr_2O_3	< d.l	< d.l

Table 4 (continued)

	Gln		Lws	Lws		Ph		Ep	Ep in Grt
			Core	Rim					
FeO_{tot}	15.62	FeO_{tot}	1.87	1.89	FeO_{tot}	5.18	FeO_{tot}	14.92	12.73
MnO	0.09	MnO	< d.l	< d.l	MnO	< d.l	MnO	0.63	0.41
MgO	9.93	MgO	< d.l	0.09	MgO	4.1	MgO	0.03	0.05
CaO	1.16	CaO	17.2	17.31	CaO	0.09	CaO	22.00	22.32
Na_2O	6.26	Na_2O	< d.l	< d.l	Na_2O	< d.l	Na_2O	< d.l	< d.l
K_2O	0.01	K_2O	< d.l	< d.l	K_2O	10.72	K_2O	< d.l	< d.l
Total	95.32	Total	88.27	88.35	Total	94.83	Total	95.68	96.79
Equiv. O/Cation	23/13	Equiv. O	8	8	Equiv. O	11	Equiv. O	12.5	12.5
Si	7.90	Si	1.99	1.99	Si	3.50	Si	3.06	3.07
Ti	0.01	Ti	0.00	0.01	Ti	0.01	Ti	0.01	0.00
Al	1.12	Al	1.95	1.93	Al	1.86	Al	2.18	2.31
Fe	1.86	Fe^{3+}	0.08	0.08	Cr	0.01	Cr	0.00	0.00
Mn	0.01	Ca	0.97	0.98	Fe	0.30	Fe	1.06	0.88
Mg	2.11				Mn	0.00	Mn	0.05	0.03
Ca	0.18				Mg	0.42	Mg	0.00	0.01
Na	1.73				Ca	0.01	Ca	1.99	1.97
K	0.00				Na	0.00			
					K	0.93			
Mg#	0.71								
Fe^{3+}#	0.49						$Fe^{3+}/(Fe^{3+}+Al)$	0.33	0.26

FeO_{tot} = All iron is reported as FeO wt%; < d.l. = less than detection limit (i.e., analyzed but not detected); Mg# = $Mg/(Mg+Fe^{2+})$; Fe^{3+}# = $Fe^{3+}/(Fe^{3+}+Al^{vi})$; Charge balance indicates presence of little to no Fe^{2+} in lawsonite; Ps = Pistacite content ($Fe^{3+}/(Fe^{3+}+Al)$)

Table 5 Measured and calculated bulk rock compositions of metagabbro and metabasalt

Sample	Glaucophane-bearing Metagabbro					Glaucophane-free Metagabbro			
	SV08-507					SV08-505 (Lws Metagabbro)			SV08-511A (Lws-Ep Metagabbro)
	Measured	Stage1	Stage 1*	Stage 2	Stage 2*	Measured	CAL	CAL*	Measured
SiO_2	48.61	50.79	47.63	50.93	47.73	45.94	46.71	42.62	41.38
TiO_2	1.07	0.07	0.06	0.07	0.06	0.24	0.09	0.08	0.32
Al_2O_3	14.72	22.81	20.54	22.83	20.54	15.98	27.42	24.01	17.89
FeO_{tot}	8.61	5.79	5.61	5.57	5.39	4.26	1.90	1.82	4.84
MnO	0.14	0.08	0.08	0.04	0.04	0.10	0.05	0.05	0.16
MgO	6.39	3.78	3.70	3.80	3.72	10.56	5.25	5.24	10.60
CaO	10.63	12.86	11.67	12.91	11.71	15.52	18.20	16.29	17.15
Na_2O	3.79	2.62	2.58	2.65	2.61	1.66	0.33	0.32	0.30
K_2O	0.61	1.19	1.11	1.20	1.13	0.06	0.03	0.03	0.03
P_2O_5	0.02					0.01			0.02
LOI	4.75					5.66			6.84
H_2O*			6.50		6.57			9.46	
H_2O^M		6.4–6.6		6.4–6.7			8.3–8.7		
Total	94.59	100.00	99.50	100.00	99.49	94.33	99.98	99.92	92.70
Sample	Metabasalt layers								
	SV08-509								
	Measured	BLS (CAL)	BLS (CAL*)	BLS (Stage1)	BLS (Stage2)	ECL (CAL)	ECL (CAL*)	ECL (Stage 1)	ECL (Stage 2)
SiO_2	47.78	49.79	47.12	49.84	49.84	48.88	46.38	48.92	48.92
TiO_2	1.37	1.55	1.55	1.56	1.56	2.14	2.13	2.14	2.14
Al_2O_3	15.45	18.03	16.47	18.05	18.05	18.37	16.67	18.39	18.39
FeO_{tot}	10.45	11.11	10.76	10.77	10.28	9.70	9.47	9.60	8.87
MnO	0.19	0.23	0.23	0.19	0.11	0.20	0.20	0.17	0.08
MgO	5.08	5.23	5.08	5.22	5.19	4.09	3.99	4.09	4.05
CaO	9.17	9.50	8.70	9.44	9.27	11.64	10.77	11.61	11.41
Na_2O	3.78	3.87	3.77	3.87	3.87	3.99	3.93	3.99	3.99
K_2O	1.25	0.60	0.56	0.60	0.60	0.90	0.85	0.91	0.91
P_2O_5	0.10								
LOI	4.86								
H_2O*			5.59				5.52		
H_2O^M				2.6–5.0	2.5–5.4			2.0–4.5	2.0–4.7
Total	94.63	99.92	99.83	99.53	98.76	99.91	99.91	99.83	98.76

Measured = Bulk rock compositions measured from XRF; CAL = Bulk rock compositions calculated from mineral modes and compositions; Stage 1 & Stage 2 = Effective bulk rock compositions calculated for two different stages of metamorphic evolution. Stage 1 represents the compositional system equilibrated at an earlier stage than Stage 2; * = Asterisk indicates H_2O was considered as an additional chemical component in the compositional systems of CAL, Stage 1, or Stage 2 and its amount was calculated from the modes and compositions of hydrous phases; FeO_{tot} = All iron is reported as FeO wt%; LOI = H_2O determined from loss of ignition; H_2O* = H_2O calculated from hydrous mineral modes and compositions; H_2O^M = H_2O modelled from pseudosection

modelled H_2O content of 6.6–6.7 wt% (Fig. 7b). Significantly lower P (~ 1.9 GPa) and slightly higher T (~ 510 °C) were predicted from the other region of intersection at which the X_{prp} and X_{sps} isopleths of garnet overlap with the X_{ae} isopleth of omphacite (Fig. 7b). The predicted metamorphic assemblage is Ph + Grt + Gln + Omp + Lws + Rt + Qz + Chl ± Ep, and it is stable with the modelled H_2O content of 6.4 wt%. The overall range of H_2O content estimated from pseudosection modeling (6.4–6.7 wt%) is similar to the calculated range of bulk H_2O (6.5–6.6 wt%), but higher than the LOI value (4.8 wt%) (Table 5). The overall results of pseudosection modelling suggest a possible isothermal decompression with no significant change in the bulk H_2O content.

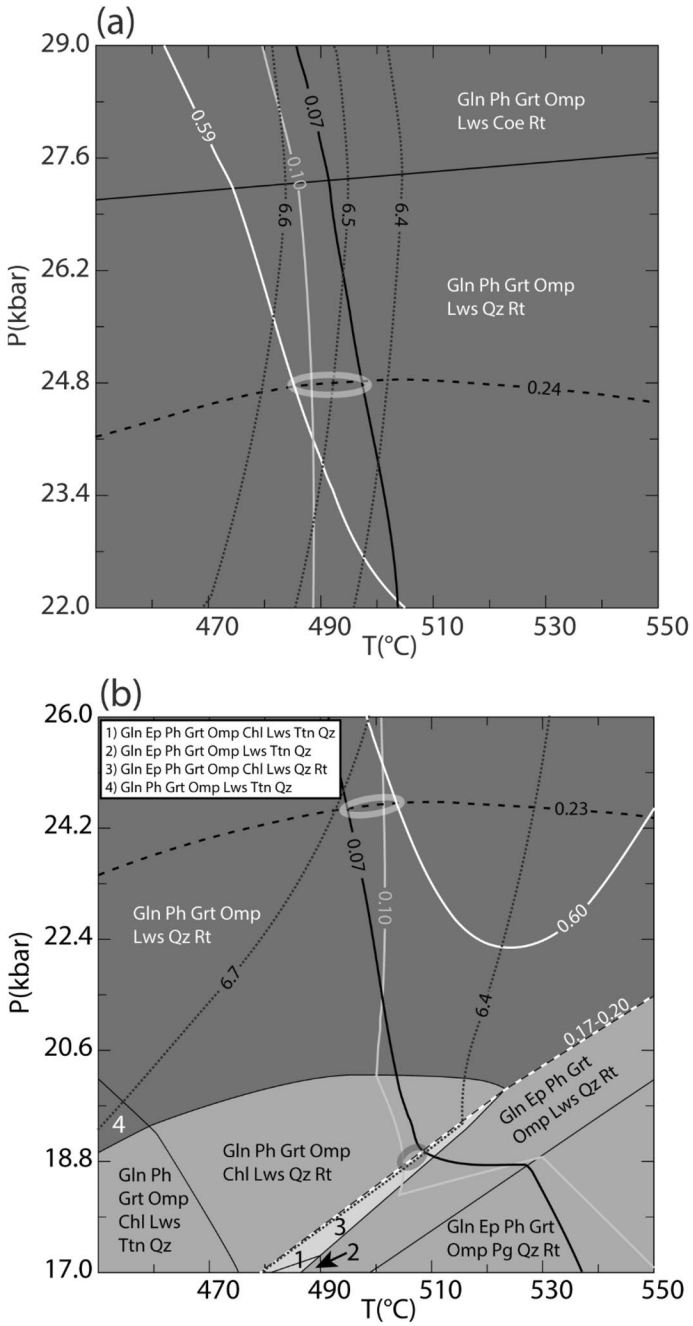

Fig. 7 P–T pseudosections constructed for glaucophane-bearing metagabbro (SV08-507), using effective bulk rock compositions calculated for two metamorphic stages. The earlier stage (Stage 1) is relevant to the growth of garnet core, and the corresponding isopleths best overlap at $X(Fe_2O_3) = 0.2$ (7a). The modelled compositional isopleths of garnet and omphacite at their rims (Stage 2) show the best intersection at $X(Fe_2O_3) = 0.3$ (7b). The ellipse indicates the field of intersection between isopleths. Black dotted lines = H_2O wt% in the modelled system; Black dashed line = X_{grs} isopleth; Black solid lines = X_{prp} isopleths; Gray solid lines = X_{sps} isopleths; White solid line = X_{alm} isopleths; White dashed lines = X_{ae} isopleths

P–T-H_2O conditions of glaucophane-free metagabbro (SV08-505)

In the phase diagram (Fig. 8), the X_{ae} isopleths for clinopyroxene were contoured, and their values correspond to the range of matrix omphacite (0.17–0.22). The estimated modal amount (10–21%) and the X_{Mg} ($Mg/Mg + Fe^{2+}$) (0.92–0.99) of matrix tremolite were also plotted in the pseudosection as additional isopleths (Fig. 8). The region of intersection of modal and compositional isopleths is relatively consistent with the mineral assemblage of the metagabbro at $X(Fe_2O_3) = 0.1$ (Fig. 8). The predicted prograde metamorphic assemblage is $Tr + Ph + Grt + Omp + Lws + Qz + Rt \pm Ep \pm Tlc$ and it is stable at ~ 580–600 °C and 2.3–2.5 GPa with 8.3–8.7 H_2O wt% (Fig. 8). The modelled H_2O content (8.3–8.7 wt%) is slightly lower than the calculated bulk H_2O content (9.5 wt%), but significantly higher than the LOI value (5.7%; Table 5).

The main discrepancy between modelled and observed minerals is the predicted presence of garnet. In contrast to the glaucophane-bearing metagabbro, the glaucophane-free metagabbro used for pseudosection modeling apparently

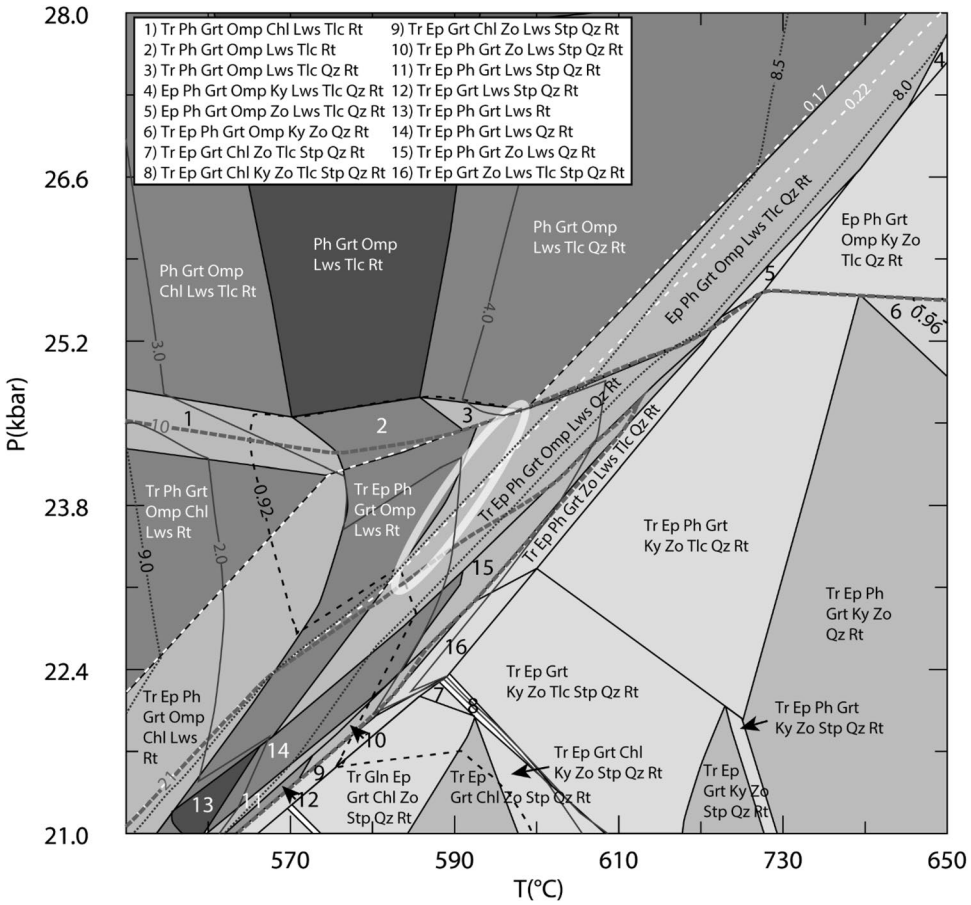

Fig. 8 P–T pseudosection constructed for glaucophane-free metagabbro (SV08-505) at $X(Fe_2O_3) = 0.1$, using effective bulk rock composition calculated from the inferred prograde/peak assemblage (Lws + Omp + Tr). An ellipse shows the region of intersection between the compositional isopleths of matrix amphibole (X_{Mg}; black dashed lines) and matrix clinopyroxene (X_{ae}; white dashed lines), and the isopleths of amphibole mode % (gray dashed lines). Black dotted lines = H_2O wt% in the modelled system; Gray solid lines = garnet mode %

lacks garnet, but the modelled composition predicts that garnet is stable across a wide range of P–T conditions (Fig. 8). However, the modelled abundance of garnet is low (3–4%), and the predicted peak P–T conditions are compatible with previous studies of lawsonite-bearing rocks in this region (550 °C, 1.5–2.4 GPa) (Davis and Whitney 2006, 2008), indicating that the pseudosection provides a reasonable view of metamorphic conditions of this rock. The discrepancy may be due to inaccuracies in thermodynamic data and/or to minor errors in the estimation of effective bulk-rock composition given the complex and heterogeneous texture of the metagabbro (Figs. 3e, f). Alternatively, garnet might have been destabilized during exhumation, as predicted in the phase diagram in which the modelled abundance of garnet significantly decreases with decreasing temperature. The modal abundances of epidote, rutile, quartz, and talc are predicted to be significantly low (<<1%), consistent with the rarity of these phases in the sample.

P–T-H_2O conditions of metabasalt (SV08-509)

Because the fine-grained metabasalt consists of layers of blueschist and eclogite, we constructed pseudosections for bulk compositions calculated for each layer, taking into account the assumptions necessary to derive an effective bulk composition. Isopleths for X_{ae} of omphacite and X_{grs}, X_{prp}, X_{alm}, and X_{sps} of garnet were contoured in each phase diagram (Figs. 9, 10). In eclogite layers, the compositional isopleths of omphacite inclusions and the corresponding isopleths of host garnet at the location of omphacite inclusions start to intersect at $X(Fe_2O_3) = 0.2$ (Stage 1; Online Resource 2). The most reasonable mineral assemblage is predicted at $X(Fe_2O_3) \geq 0.3$ within the region of overlap between X_{prp}, X_{sps} and X_{ae} isopleths (Fig. 9a, Online Resource 2). The predicted mineral assemblage (Ep + Ph + Grt + Gln + Omp + Lws + Rt ± Qz ± Chl) is stable with 2.0–4.5 wt% of water content over the range of T (490–500 °C) and P (1.8 GPa) (Fig. 9a). The later metamorphic stage, relevant to the growth of matrix omphacite and garnet rims, shows the best intersection at $X(Fe_2O_3) \geq 0.3$ (Stage 2; Online Resource 2). The field of intersection is defined by the isopleths of X_{prp}, X_{sps} and X_{ae} and it is located at 500–530 °C and ~ 1.9 GPa, with the predicted H_2O content ranging from 2.0 to 4.7 wt% (Fig. 9b). The modelled mineral assemblage (Ep + Ph + Grt + Gln + Omp + Lws + Rt ± Qz ± Chl) is consistent with the prograde assemblage present in the matrix (Fig. 9b). The compositional isopleths of garnet (X_{grs}, X_{prp}, X_{alm}, and X_{sps}) corresponding to Stages 1 and 2 consistently intersect

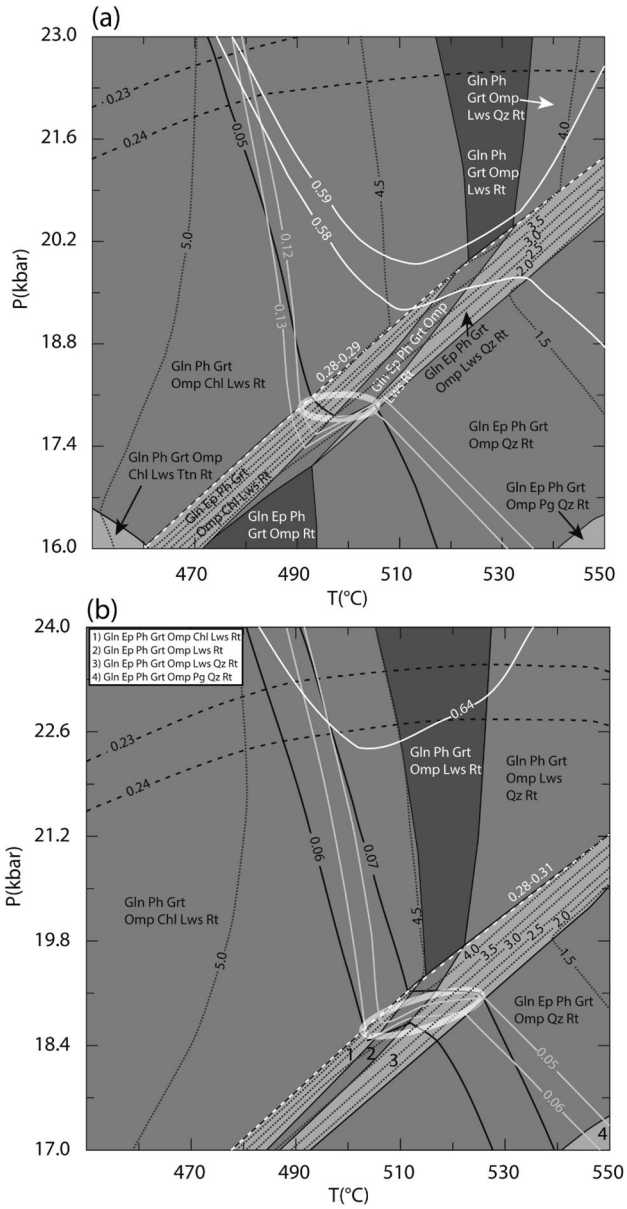

Fig. 9 P–T pseudosections constructed for an eclogite layer in metabasalt (SV08-509), using effective bulk rock compositions calculated for two metamorphic stages. The earlier stage (Stage 1) corresponds to the formation of the inclusion assemblage within garnet and the relevant compositional isopleths of omphacite inclusions and host garnet show the best intersection at $X(Fe_2O_3)=0.3$ (9a). The rim compositions of matrix omphacite and garnet, which are inferred to have been in equilibrium at the later stage of metamorphism (Stage 2), best intersect at $X(Fe_2O_3)=0.3$ (9b). Black dotted lines = H_2O wt% in the modelled system; Black dashed lines = X_{grs} isopleths; Black solid lines = X_{prp} isopleths; Gray solid lines = X_{sps}; White solid line = X_{alm} isopleths; White dashed lines = X_{ae} isopleths. The ellipse indicates the field of intersection between compositional isopleths

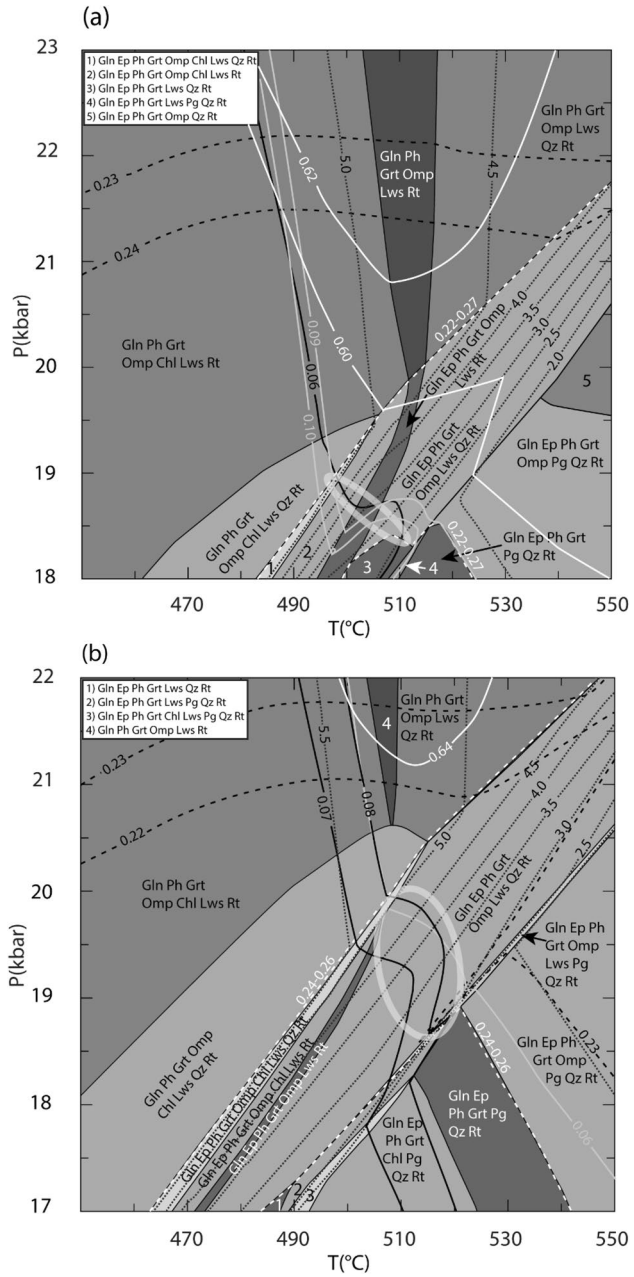

Fig. 10 P–T pseudosections constructed for the blueschist layers of interlayered metabasalt (SV08-509), using effective bulk rock compositions calculated for two metamorphic stages. The earlier stage (Stage 1) shows the best intersection at $X(Fe_2O_3)=0.25$ (10a), while the modelled isopleths relevant to the later stage of metamorphism (Stage 2) best overlap at $X(Fe_2O_3)=0.3$ (10b). The ellipse indicates the field of intersection between compositional isopleths. Black dotted lines = H_2O wt% in the modelled system; Black dashed lines = X_{grs} isopleths; Black solid lines = X_{prp} isopleths; Gray solid lines = X_{sps} isopleths; White solid line = X_{alm} isopleths; White dashed lines = X_{ae} isopleths

from $X(Fe_2O_3) \geq 0.1$ (Online Resource 2), but the predicted mineral assemblages are not in agreement with observed inclusion and matrix assemblages (e.g., the lack of chlorite in garnet, the presence of epidote in the matrix) (Figs. 9a, b).

In blueschist layers, compositional isopleths of omphacite and garnet start to overlap at $X(Fe_2O_3) = 0.1$ (Online Resource 3). However, the modelled isopleths from each effective bulk composition do not intersect in the field consistent with textural evidence at the relevant stage of metamorphism (i.e., inclusion assemblage of garnet and matrix mineral assemblage), until $X(Fe_2O_3)$ reaches 0.25 and 0.30 for the earlier and later metamorphic stages, respectively (Fig. 10, Online Resource 3). The earlier metamorphic stage (Stage 1), represented by the compositional equilibrium between omphacite inclusion and its host garnet, predicts Ep + Ph + Grt + Gln + Omp + Lws + Rt ± Qz ± Chl as a stable assemblage at 500–510 °C and ~ 1.9 GPa (Fig. 10a). The corresponding modelled water content varies from 2.6–5.0 wt% (Fig. 10a). The compositional isopleths relevant to the later stage of metamorphism (Stage 2) intersect in the field of Ep + Ph + Grt + Gln + Omp + Lws + Qz + Rt ± Chl at 510–520 °C and 1.9–2.0 GPa with 2.5–5.4 wt% as the predicted water content in the system (Fig. 10b). The compositional isopleths of garnet (X_{grs}, X_{prp}, X_{alm}, and X_{sps}), relevant to Stages 1 and 2, overlap each other from $X(Fe_2O_3) \geq 0.1$ (Online Resource 3) but in fields inconsistent with textural evidence (e.g., the lack of chlorite in garnet, the presence of epidote in the matrix) (Fig. 10a, b).

The calculated water content of eclogite layers is 5.5 wt%, which is only slightly higher than the upper range of H_2O content determined from pseudosection modeling (2.0–4.7 wt%). Similar H_2O content was estimated from blueschist layers (5.6 wt%), and it corresponds to the range of water content (2.5–5.4 wt%) predicted from pseudosection calculations.

Blueschist layers record similar P and T (1.9–2.0 GPa, 500–520 °C) as eclogite layers (1.8–1.9 GPa, 490–530 °C). Both the blueschist and eclogite layers likely remained close to the lawsonite-epidote stability boundary at prograde conditions with no significant change in bulk $X(Fe_2O_3)$: eclogite = 0.3 and blueschist = 0.25–0.30.

Uncertainty of the results of pseudosection modeling

Caution is needed when interpreting the results of pseudosection modeling, owing to the assumptions made in calculating the phase diagrams. One such assumption concerns the estimate of effective bulk-rock composition, because the complex and heterogeneous texture of metagabbro (Fig. 3) can cause minor errors in the estimates of mineral modes and consequently in the calculation of effective bulk-rock composition. To minimize such error, our study focused, where possible, on areas of the thin sections that lacked relict igneous minerals and secondary replacement textures.

Another assumption concerns the amount of Fe^{3+} present in the rock. The ferric iron content of omphacite was stoichiometrically determined based on WDS compositional analyses. Other studies have found that the ratio of $Fe^{3+}/(Fe^{3+} + Fe^{2+})$ calculated from electron microprobe analyses does not match the ferric iron ratio measured directly by Mössbauer spectroscopy (Sobolev et al. 1999; Proyer et al. 2004). If such a discrepancy exists in this case, the results of pseudosection modeling would provide erroneous estimates of the P–T-H_2O conditions. We also used the Fe^{3+}-free solution model of garnet (Holland and Powell 1998) in the pseudosection calculations. We chose this model instead of a Fe^{3+}-bearing solution model (White et al. 2007; Malaspina et al. 2009), as no appreciable amount of Fe^{3+} was stoichiometrically determined in the garnet analyzed in this study. Furthermore, the Fe^{3+}-bearing solution model gives unreliable results in the case of spessartine-rich garnet. Even though the analyzed garnet is relatively lower in Mn than Ca, the Mn concentration is higher than the Mg and stoichiometrically derived Fe^{3+} concentrations (Tables 2, 4). Our preliminary results suggest that this appreciable amount of Mn in the garnet erroneously predicts spessartine as a separate stable phase when the Fe^{3+}-bearing solution model was applied. Therefore, the influence of Fe^{3+} on garnet stability was neglected. Despite these uncertainties and assumptions, the P–T conditions we modelled correspond well with the previous estimates for metabasalt (Davis and Whitney, 2006), suggesting a reliable approximation of the ferric iron content of omphacite and the insignificant influence of Fe^{3+} on garnet stability in these rocks.

Discussion

Sivrihisar metagabbro contains a texturally complex mineral assemblage that differs from that of associated fine-grained metabasalt—e.g., the presence of relict igneous clinopyroxene and the absence or scarcity of garnet and glaucophane in metagabbro. Such differences in texture and mineral assemblage between metabasalt and metagabbro may result from differences in P–T histories, grain size, bulk composition, and/or availability of H_2O during their metamorphic evolution. The following discussion explores the factors that may have led to the significant differences between Sivrihisar metagabbro and metabasalt.

Effects of metamorphic conditions, grain size, and deformation on metamorphic reactions

Both metagabbro and metabasalt record lawsonite-eclogite facies conditions, but only the metagabbro preserves relict

igneous clinopyroxene. Metamorphic temperatures of Sivrihisar metagabbro did not exceed 600 ℃, but incomplete gabbro-eclogite transformation has been observed in metagabbro from other localities that reached 700–900 °C and 1.5–2.8 (Mørk 1985; Indares and Rivers 1995; Zhang and Liou 1997; John and Schenk 2003). Based on this comparison and the general similarity in P–T conditions of metagabbro and metabasalt, temperature was not the major control on differences in mineral assemblages and textures.

Alternatively, metagabbro did not react completely owing to the coarser grain size of its protolith compared to metabasalt, as has been reported for other metamorphic rocks with coarse-grained protoliths (e.g., Reynard and Ballèvre 1988; Lardeaux and Spalla 1991; Hacker 1996). The common occurrence of coarse-grained relict clinopyroxene (0.5–18 mm) in Sivrihisar metagabbro is the most clear indication of the coarse-grained protolith, and this characteristic likely lowered the volume fraction of grain boundary junctions that function as diffusional pathways (Brady 1983; Carlson and Gordon 2004).

Although metagabbro did not completely react to eliminate protolith phases during prograde metamorphism, metagabbro is more extensively retrogressed than metabasalt, as seen by the high modal abundance of secondary glaucophane and chlorite as well as by the presence of calcite veins (Table 1). In contrast, the analyzed metabasalt exposed in close proximity to metagabbro nearly lacks secondary minerals (Table 1), although some metabasites in the region show variable amounts of retrogression (e.g., partial replacement of garnet by chlorite). Such different degrees of retrogression may result from a difference in rheological behavior between metagabbro and metabasalt. In our sample locality, eclogite-facies metagabbro typically occurs as small (< 1 m) pods, whereas associated metabasalt is typically present in the form of layers. As noted in a previous study on Sivrihisar metabasaltic pods (Davis and Whitney 2008), the eclogite pods likely formed during an early stage of exhumation. Subsequent deformation tended to be partitioned to the pod margins instead of surrounding layers owing to the rheological contrast between the more rigid pods and the more ductile layers. Metagabbro pods also likely experienced such localized deformation, which eventually enhanced their retrogression to form post-peak minerals that wrap around the rims of metagabbro pods during exhumation as compared to co-existing metabasalt layers. Such localized deformation is well evidenced by glaucophane + garnet-bearing metagabbro, which is rimmed by retrograde glaucophane + lawsonite-rich blueschist layers (Fig. 3b).

The influence of bulk rock composition on metamorphic reactions

The bulk rock composition of glaucophane + garnet-absent metagabbro is significantly enriched in CaO and MgO contents but depleted in Na_2O and FeO_{tot} contents relative to coexisting glaucophane + garnet-bearing metagabbro and metabasalt (Table 5). To illustrate the influence of bulk-rock composition on mineral paragenesis and thus to demonstrate the distinctive HP/LT mineral assemblage of glaucophane + garnet-free metagabbro, we constructed cumulative phase mode diagrams for two metagabbro samples with different peak mineral assemblages (with and without garnet + glaucophane). At the modelled peak P–T conditions, the cumulative mineral modes of each sample were plotted as a function of three bulk compositional factors that show major differences between the two samples: (1) Na_2O mol%; (2) CaO mol %; and (3) $X_{Mg} = MgO/(MgO + FeO_{tot})$ (Fig. 11). Each compositional factor was evaluated to determine whether or not it can induce systematic changes in the mineral modes and such changes are consistently predicted in the two samples. Na_2O and CaO mol% were increased by more than 150% of the original bulk concentrations.

The diagrams consistently predict that omphacite mode increases, whereas lawsonite, amphibole (Tr/Gln), quartz, and talc modes decrease with increasing Na_2O mol% (Figs. 11a, b). A continuous increase in CaO mol%, in contrast, leads to non-systematic changes in omphacite modal abundance, which differs for each sample (Figs. 11c, d). With increasing CaO mol%, omphacite mode in the Na-richer garnet + glaucophane-bearing metagabbro (SV08-507) is initially decreased by the stabilization of lawsonite and glaucophane, and subsequently increased by the breakdown of glaucophane and/or lawsonite (Fig. 11c). A following decrease in the omphacite mode is primarily associated with increasing formation of garnet and other Ca-bearing phases (Fig. 11c). In the Ca-richer garnet + glaucophane-free metagabbro (SV08-505), on the other hand, omphacite mode increases, but subsequently decreases owing to the stabilization of garnet (and possibly vesuvianite; Figs. 11d). These non-systematic changes in omphacite mode with increasing CaO mol% contrast with previous results suggesting that higher bulk X_{Ca} ($CaO/(CaO + Na_2O)$) favors the development of an eclogitic assemblage (omphacite + garnet) in metabasalt (e.g., Gomez-Pugnaire et al. 1997; Vitale Brovarone et al. 2011; Wei and Clarke 2011). Our results highlight the importance of Na_2O content of the gabbro protolith as an additional significant factor (Figs. 11a, b). These results are further supported by the higher omphacite mode observed in the Na-richer metagabbro sample (SV08-507) as compared to the Ca-richer metagabbro samples (SV08-505, 511A) (Table 1). Alternatively, factors other than bulk-rock composition (e.g., coarse-grain size) might have prohibited and thus primarily controlled the formation of omphacite in the analyzed metagabbro samples. In such cases, a positive correlation between omphacite mode and bulk X_{Ca} can be lost.

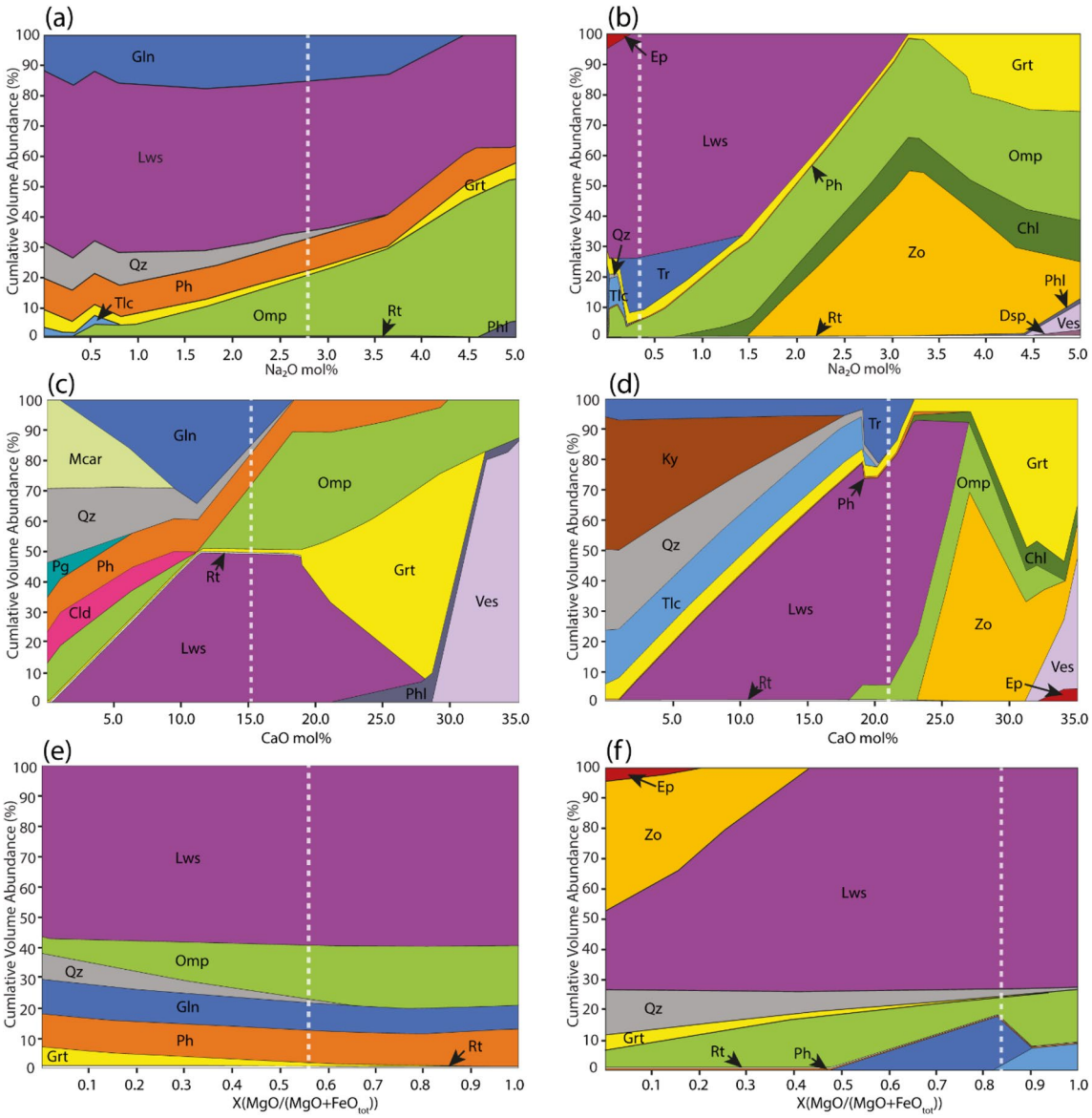

Fig. 11 Cumulative phase mode diagrams of two metagabbro samples with different peak mineral assemblages. Modal abundances of all stable phases are plotted at modelled peak P–T conditions as a function of bulk Na mol% (**a**, **b**), bulk Ca mol% (**c**, **d**), and bulk X_{Mg} ($MgO/(MgO+FeO_{tot})$) (**e**, **f**). The vertical dotted line in each diagram indicates the relevant bulk content or compositional ratio of glaucophane-bearing metagabbro (**a, c, e**; SV08-507) and glaucophane-absent metagabbro (**b**, **d**, **f**; SV08-505)

Garnet mode predicted in the diagrams consistently decreases with increasing X_{Mg} (Figs. 11e, f). This suggests that gabbro protoliths may tend to develop lesser amounts of garnet during eclogite-facies metamorphism when enriched in bulk MgO relative to FeO_{tot}. If that was the case, the absence of garnet in one of the metagabbro samples (SV08-505) might be attributed to the Mg-richer nature of the protolith ($X_{Mg} = 0.84$) compared to the protolith of garnet-bearing metagabbro (SV08-507; $X_{Mg} = 0.58$). Although the modal abundance of garnet also depends on bulk CaO, it shows no systematic changes in the diagrams (Figs. 11c, d).

Prograde P–T estimates of spatially associated glaucophane-rich and omphacite-rich layers of metabasalt are similar, indicating that these blueschists and eclogites are cofacial. According to the calculated bulk compositions, the main difference between blueschist and eclogite layers is that blueschist layers are Fe-richer (~ 11% vs. ~ 9% FeO_{tot}) and eclogite layers are Ca-richer (~ 11% vs. ~ 9% CaO) (Table 5). Higher bulk Ca in eclogite compared to associated blueschist is consistent with other studies of Sivrihisar metabasite (Davis and Whitney, 2006) and data from other localities (Wei and Clarke, 2011). Therefore, the fine-scale variations in mineral assemblage are likely the result of compositional

variation. Interestingly, our results of pseudosection modelling indicate no significant difference in bulk $X(Fe_2O_3)$ and H_2O content at prograde P–T conditions between the blueschist and eclogite layers.

The role of H_2O on metamorphic reactions

The amount of H_2O estimated at the prograde P–T conditions is the highest in glaucophane + garnet-absent metagabbro (8.3–8.7 wt%). Lower H_2O content was predicted for glaucophane + garnet-bearing metagabbro (6.4–6.7 wt%), but it is still higher than the range predicted for the blueschist (2.5–5.4 wt%) and eclogite layers (2.0–4.7 wt%) in metabasalt. If H_2O content at prograde conditions primarily controlled metamorphic transformation into the HP/LT mineral assemblage, metagabbro should have been converted into eclogite at least to an extent similar to that of metabasalt.

To better understand the role of H_2O in the transformation of gabbro to metagabbro, we calculated the cumulative mineral abundance as a function of changing bulk H_2O content at fixed peak P–T conditions. In both metagabbro samples modelled, Ky + Zo/Ep + Qz + Ph ± Kfs were predicted to be stable in addition to garnet and omphacite over the range of bulk H_2O content, which is lower than the amount required for H_2O-excess conditions in pseudosection modeling (Fig. 12). The predicted assemblage partially corresponds to a commonly reported assemblage for eclogite-facies metagabbro (Ky + Zo + Qz + Grt ± Ab ± Ph) in which igneous plagioclase relics may be preserved (Wayte et al. 1989; Zhang and Liou 1997; Wain et al. 2001; Miller et al. 2007; Proyer and Postl 2010). With increasing H_2O content, the modal abundance of hydrous phases, such as lawsonite and/or amphibole, increases at the expense of Grt + Ky + Zo/Ep + Qz ± Kfs, which become nearly absent or present in small amounts at H_2O-excess condition (Fig. 12). Based on the results of these phase diagrams, a true eclogite assemblage dominated by omphacite and garnet is produced at a low bulk H_2O content, whereas increased H_2O content results in the breakdown of garnet. This is consistent with previous results of pseudosection modeling of variably eclogitized metagabbro in other localities (e.g., Rebay et al. 2010; Schorn and Diener 2017). In this respect, the absence or rarity of garnet in the analyzed metagabbro samples might be the result of a high bulk H_2O content at the peak condition, combined with additional influences from its Mg-richer bulk composition ($X_{Mg} = 0.58–0.84$) compared to nearby metabasalt ($X_{Mg} = 0.50$) and from garnet-breakdown reactions during exhumation (Fig. 8). However, the occurrence of relict igneous clinopyroxene still implies an incomplete gabbro-eclogite transformation, which might have been hindered, in part, by coarse grain size.

Implications for formation of garnet-absent assemblages in eclogite facies metabasite

Eclogite-facies metagabbro consisting of abundant omphacite but no or very rare garnet, such as occurs in the Sivrihisar Massif, resembles omphacitites that have been reported as pods and/or veins in other HP/LT metamorphic complexes (Och et al. 2003; Shi et al. 2010; Fu et al. 2012; Shigeno et al. 2012; Vitale Brovarone 2013). Omphacitites have been suggested to form by either metasomatic replacement of metamafic protolith or by direct precipitation from fluids (Shi et al. 2010; Vitale Brovarone 2013). Our results suggest that Sivrihisar omphacite-bearing, garnet-absent (or rare) assemblages might have originated from the prograde metamorphism of gabbro protoliths that

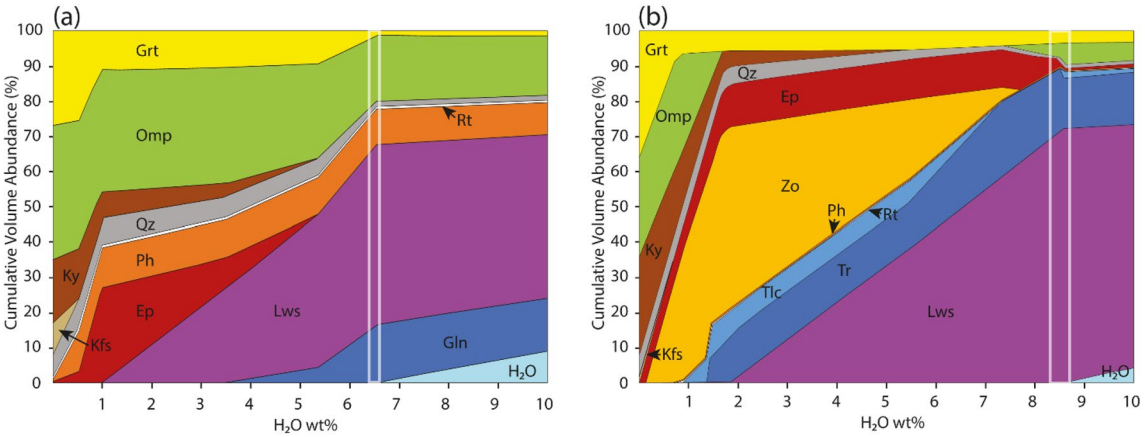

Fig. 12 Cumulative phase mode diagrams of glaucophane-bearing metagabbro (12a; SV08-507) and glaucophane-free metagabbro (12b; SV08-505). Modal abundances of all stable phases are plotted at modelled peak P–T conditions as a function of bulk H_2O wt%. The rectangular area in each diagram indicates the relevant range of bulk H_2O content modelled at H_2O-excess condition

had sufficient Na_2O, MgO, and H_2O to stabilize omphacite but destabilize garnet during HP/LT metamorphism. In this scenario, hydrothermal alteration of oceanic crust during seafloor metamorphism is a likely process that leads to the formation of omphacitite; with increasing fluid-rock interaction depths, mafic protoliths typically gain CaO and MgO relative to Na_2O and K_2O (Coleman 1963; Seyfried et al. 1991; Miller et al. 2000; Li et al. 2004). If that was the case, the protoliths of omphacite-rich metagabbro (SV08-507) and garnet + glaucophane-free metagabbro (SV08-505, 511A) might have been, in part, influenced by shallow and deep hydrothermal alterations, respectively, given the higher Na_2O and K_2O contents of the former relative to the latter (Table 5).

Conclusions

This study provides new petrographic, geochemical, and pseudosection analyses of coarse-grained and fine-grained HP/LT metabasite (inferred metagabbro and metabasalt, respectively) that are well exposed in the Sivrihisar Massif, Turkey. Metagabbro consists of a texturally complex mineral assemblage, including relict igneous clinopyroxene, HP/LT metamorphic minerals (lawsonite + omphacite ± garnet ± glaucophane ± phengite), tremolite, rutile, and retrograde minerals (e.g., albite, epidote, chlorite, and calcite). In contrast, metabasalt consists of alternating lawsonite blueschist and eclogite layers with abundant garnet and lawsonite and varying amounts of sodic amphibole and omphacite. Blueschist and eclogite layers are interpreted to be cofacial at lawsonite eclogite conditions and to have similar H_2O contents (2.0–5.4 wt%). Lawsonite-eclogite facies metagabbro has higher peak metamorphic H_2O content (6.4–8.7 wt%) than coexisting metabasalt that records similar P–T conditions. The H_2O-rich metamorphic environment may have created unfavorable conditions for garnet formation in eclogite-facies metagabbro, accounting for the sparse to absent garnet in Sivrihisar metagabbro, similar to observations from omphacite-rich, garnet-absent mafic rocks in other subduction complexes. Other factors (i.e., coarse-grain size and Mg-rich bulk-rock composition) also likely contributed to the incomplete transformation of metagabbro, and these eventually led to the differences in reaction history and peak mineral assemblages in metagabbro relative to metabasalt during subduction.

Acknowledgements We would like to thank Anette von der Handt for her instruction during electron microprobe analyses. We also gratefully acknowledge D. Rubatto and two anonymous reviewers for their constructive reviews of a preliminary version of the manuscript. This work was funded by NSF grant EAR-1949895 and by support from the College of Science and Engineering of the University of Minnesota.

References

Angiboust S, Agard P, Jolivet L, Beyssac O (2009) The Zermatt-Saas ophiolite: the largest (60-km wide) and deepest (c. 70–80 km) continuous slice of oceanic lithosphere detached from a subduction zone? Terra Nova 21:171–180

Angiboust S, Langdon R, Agard P et al (2012) Eclogitization of the Monviso ophiolite (W. Alps) and implications on subduction dynamics. J Metamorph Geol 30:37–61

Brady JB (1983) Intergranular diffusion in metamorphic rocks. Am J Sci 283:181–200

Brodie KH, Rutter EH (1985) On the relationship between deformation and metamorphism, with special reference to the behavior of basic rocks. In: Thompson AB, Rubie DC (eds) Metamorphic reactions: kinetics, textures, and deformation. Springer, New York, pp 138–179

Carlson WD, Gordon CL (2004) Effects of matrix grain size on the kinetics of intergranular diffusion. J Metamorph Geol 22:733–742

Çetinkaplan M, Candan O, Oberhänsli R, Bousquet R (2008) Pressure–temperature evolution of lawsonite eclogite in Sivrihisar; Tavşanlı Zone-Turkey. Lithos 104:12–32

Coleman RG (1963) Serpentinites, rodingites, and tectonic inclusions in Alpine-type mountain chains. Geol Soc Am Spec Pap 73:130–131

Connolly JAD (1990) Multivariable phase diagrams; an algorithm based on generalized thermodynamics. Am J Sci 290:666–718

Davis PB, Whitney DL (2006) Petrogenesis of lawsonite and epidote eclogite and blueschist, Sivrihisar Massif, Turkey. J Metamorph Geol 24:823–849

Davis PB, Whitney DL (2008) Petrogenesis and structural petrology of high-pressure metabasalt pods, Sivrihisar, Turkey. Contrib Mineral Petrol 156:217–241

De Ronde AA, Stünitz H (2007) Deformation-enhanced reaction in experimentally deformed plagioclase-olivine aggregates. Contrib Mineral Petrol 153:699–717

Evans TP (2004) A method for calculating effective bulk composition modification due to crystal fractionation in garnet-bearing schist: implications for isopleth thermobarometry. J Metamorph Geol 22:547–557

Federico L, Crispini L, Scambelluri M, Capponi G (2007) Different PT paths recorded in a tectonic mélange (Voltri Massif, NW Italy): implications for the exhumation of HP rocks. Geodin Acta 20:3–19

Fornash KF, Whitney DL (2020) Lawsonite-rich layers as records of fluid and element mobility in subducted crust (Sivrihisar Massif, Turkey). Chem Geol 533:119356

Fornash KF, Cosca MA, Whitney DL (2016) Tracking the timing of subduction and exhumation using $^{40}Ar/^{39}Ar$ phengite ages in blueschist- and eclogite-facies rocks (Sivrihisar, Turkey). Contrib Mineral Petrol 171:67

Fornash KF, Whitney DL, Seaton NCA (2019) Lawsonite composition and zoning as an archive of metamorphic processes in subduction zones. Geosphere 15:24–46

Fry N, Barnicoat AC (1987) The tectonic implications of high-pressure metamorphism in the western Alps. J Geol Soc London 144:653–659

Fu B, Paul B, Cliff J et al (2012) O-Hf isotope constraints on the origin of zircon in high-pressure mélange blocks and associated matrix rocks from Tinos and Syros, Greece. Eur J Mineral 24:277–287

Gaidies F, Abart R, de Capitani C et al (2006) Characterization of polymetamorphism in the Austroalpine basement east of the Tauern Window using garnet isopleth thermobarometry. J Metamorph Geol 24:451–475

Gomez-Pugnaire MT, Karsten L, Sanchez-Vizcaino VL (1997) Phase relationships and P-T conditions of coexisting

eclogite-blueschists and their transformation to greenschist-facies rocks in the Nerkau Complex (Northern Urals). Tectonophysics 276:195–216

Green E, Holland T, Powell R (2007) An order-disorder model for omphacitic pyroxenes in the system jadeite-diopside-hedenbergite-acmite, with applications to eclogitic rocks. Am Mineral 92:1181–1189

Green ECR, White RW, Diener JFA et al (2016) Activity-composition relations for the calculation of partial melting equilibria in metabasic rocks. J Metamorph Geol 34:845–869

Groppo C, Castelli D (2010) Prograde P-T Evolution of a Lawsonite Eclogite from the Monviso Meta-ophiolite (Western Alps): Dehydration and Redox Reactions during Subduction of Oceanic FeTi-oxide Gabbro. J Petrol 51:2489–2514

Hacker BR (1996) Eclogite formation and the rheology, buoyancy, seismicity, and H_2O content of oceanic crust. In: Bebout GE, Scholl DW, Kirby SH, Platt JP (eds) Subduction: top to bottom, geophysical monograph 96. American Geophysical Union, Washington, pp 337–346

Holland TJB, Powell R (1998) An internally consistent thermodynamic data set for phases of petrological interest. J Metamorph Geol 16:309–343

Holland T, Baker J, Powell R (1998) Mixing properties and activity-composition relationships of chlorites in the system MgO-FeO-Al_2O_3-SiO_2-H_2O. Eur J Mineral 10:395–406

Indares A, Rivers T (1995) Textures, metamorphic reactions and thermobarometry of eclogitized metagabbros: a proterozoic example. Eur J Mineral 7:43–56

John T, Schenk V (2003) Partial eclogitisation of gabbroic rocks in a late Precambrian subduction zone (Zambia): prograde metamorphism triggered by fluid infiltration. Contrib Mineral Petrol 146:174–191

Katzir Y, Avigad D, Matthews A et al (2000) Origin, HP/LT metamorphism and cooling of ophiolitic mélanges in southern Evia (NW Cyclades), Greece. J Metamorph Geol 18:699–718

Kulaksız S (1978) Sivrihisar kuzeybatı eklojitleri. Yerbilimleri 4:89–94

Lardeaux JM, Spalla MI (1991) From granulites to eclogites in the Sesia zone (Italian Western Alps): a record of the opening and closure of the Piedmont ocean. J Metamorph Geol 9:35–59

Lardeaux JM, Nisio P, Boudeulle M (1987) Deformational and metamorphic history at the Lago Superiore area of the Monviso ophiolitic complex (Italian Western Alps): a record of subduction-collision cycle. Ofioliti 12:479–502

Li XP, Rahn M, Bucher K (2004) Metamorphic processes in Rodingites of the Zermatt-Saas Ophiolites. Int Geol Rev 46:28–51

Malaspina N, Poli S, Fumagalli P (2009) The oxidation State of Metasomatized Mantle Wedge: insights from C–O–H-bearing Garnet Peridotite. J Petrol 50:1533–1552

Meyer J (1983) Mineralogie und Petrologie des Allalingabbros. Dissertation, University of Basel

Miller JA, Buick IS, Cartwright I (2000) Textural implications of high-pressure fluid flow controlled by pre-subduction deformation and alteration patterns. J Geochem Explor 69–70:551–555

Miller C, Zanetti A, Thöni M, Konzett J (2007) Eclogitisation of gabbroic rocks: redistribution of trace elements and Zr in rutile thermometry in an Eo-Alpine subduction zone (Eastern Alps). Chem Geol 239:96–123

Mørk MBE (1985) A gabbro to eclogite transition on Flemsøy, Sunnmøre, western Norway. Chem Geol 50:283–310

Mulcahy SR, Vervoort JD, Renne PR (2014) Dating subduction-zone metamorphism with combined garnet and lawsonite Lu-Hf geochronology. J Metamorph Geol 32:515–533

Och DJ, Leitch EC, Caprarelli G, Watanabe T (2003) Blueschist and eclogite in tectonic mélange, Port Macquarie, New South Wales, Australia. Mineral Mag 67:609–624

Okay AI (1980) Mineralogy, petrology, and phase relations of glaucophane-lawsonite zone blueschists from the Tavşanli Region, Northwest Turkey. Contrib Mineral Petrol 72:243–255

Okay AI (1982) Incipient blueschist metamorphism and metasomatism in the Tavşanli region, Northwest Turkey. Contrib Mineral Petrol 79:361–367

Okay AI (1986) High-pressure/low-temperature metamorphic rocks of Turkey. In: Evans BW, Brown EH (eds) Blueschists and Eclogites. Geological Society of America Memoirs, Texas, pp 333–347

Okay AI, Kelley SP (1994) Tectonic setting, petrology and geochronology of jadeite glaucophane and chloritoid glaucophane schists from north-west Turkey. J Metamorph Geol 12:455–466

Okay AI, Whitney DL (2010) Blueschists, ophiolites and suture zones in northwest turkey: a review and a field excursion guide. Ofioliti 35:131–172

Plunder A, Agard P, Chopin C, Okay AI (2013) Geodynamics of the Tavşanlı zone, western Turkey: insights into subduction/obduction processes. Tectonophysics 608:884–903

Pognante U (1991) Petrological constraints on the eclogite-and blueschist-facies metamorphism and P-T-t paths in the western Alps. J Metamorph Geol 9:5–17

Pognante U, Kienast JR (1987) Blueschist and Eclogite transformations in Fe-Ti Gabbros: a case from the Western Alps Ophiolites. J Petrol 28:271–292

Proyer A, Postl W (2010) Eclogitized Gabbros from Gressenberg, Koralpe, Austria: transformation phenomena and their interpretation. Mitteilungen des naturwissenschaftlichen Vereines für Steiermark 140:45–67

Proyer A, McCammon C, Dachs E (2004) Pitfalls in geothermobarometry of eclogites: Fe^{3+} and changes in the mineral chemistry of omphacite at ultrahigh pressures. Contrib Mineral Petrol 147:305–318

Rebay G, Powell R, Diener JFA (2010) Calculated phase equilibria for a MORB composition in a P-T range, 450–650 C and 18–28 kbar: the stability of eclogite. J Metamorph Geol 28:635–645

Reynard B, Ballèvre M (1988) Coexisting amphiboles in an eclogite from the Western Alps: new constraints on the miscibility gap between sodic and calcic amphiboles. J Metamorph Geol 6:333–350

Rubie DC (1998) Disequilibrium during metamorphism: the role of nucleation kinetics. In: Treloar PJ, O'Brien P (eds) What drives metamorphism and metamorphic reactions? Geological Society, London, pp 199–214

Sandrone R, Leardi L, Rossetti P, Compagnoni R (1986) P-T conditions for the eclogitic re-equilibration of the metaophiolites from Val d'Ala di Lanzo (internal Piemontese zone, Western Alps). J Metamorph Geol 4:161–178

Schorn S, Diener JFA (2017) Details of the gabbro-to-eclogite transition determined from microtextures and calculated chemical potential relationships. J Metamorph Geol 35:55–75

Seyfried WE, Ding K, Berndt ME (1991) Phase equilibria constraints on the chemistry of hot spring fluids at mid-ocean ridges. Geochim Cosmochim Acta 55:3559–3580

Sherlock S, Sarah S, Simon K et al (1999) ^{40}Ar-^{39}Ar and Rb-Sr geochronology of high-pressure metamorphism and exhumation history of the Tavşanli Zone, NW Turkey. Contrib Mineral Petrol 137:46–58

Shi G, Jiang N, Wang Y et al (2010) Ba minerals in clinopyroxene rocks from the Myanmar jadeitite area: implications for Ba recycling in subduction zones. Eur J Mineral 22:199–214

Shigeno M, Mori Y, Shimada K, Nishiyama T (2012) Origin of omphacitites from the Nishisonogi metamorphic rocks, western Kyushu, Japan: comparison with jadeitites. Eur J Mineral 24:247–262

Sobolev VN, McCammon CA, Taylor LA et al (1999) Precise Mössbauer milliprobe determination of ferric iron in rock-forming

minerals and limitations of electron microprobe analysis. Am Mineral 84:78–85
Teyssier C, Whitney DL, Toraman E, Seaton NCA (2010) Lawsonite vorticity and subduction kinematics. Geology 38:1123–1126
Vitale Brovarone A (2013) Lawsonite-bearing omphacitites from Alpine Corsica (France). Int J Earth Sci 102:1377–1379
Vitale Brovarone A, Groppo C et al (2011) Coexistence of lawsonite-bearing eclogite and blueschist: phase equilibria modelling of Alpine Corsica metabasalts and petrological evolution of subducting slabs. J Metamorph Geol 29:583–600
Wain AL, Waters DJ, Austrheim H (2001) Metastability of granulites and processes of eclogitisation in the UHP region of western Norway. J Metamorph Geol 19:609–625
Wayte GJ, Worden RH, Rubie DC, Droop GTR (1989) A TEM study of disequilibrium plagioclase breakdown at high pressure: the role of infiltrating fluid. Contrib Mineral Petrol 101:426–437
Wei CJ, Clarke GL (2011) Calculated phase equilibria for MORB compositions: a reappraisal of the metamorphic evolution of lawsonite eclogite. J Metamorph Geol 29:939–952
White RW, Powell R, Holland TJB (2007) Progress relating to calculation of partial melting equilibria for metapelites. J Metamorph Geol 25:511–527
Whitney DL, Davis PB (2006) Why is lawsonite eclogite so rare? Metamorphism and preservation of lawsonite eclogite, Sivrihisar, Turkey. Geology 34:473–476
Whitney DL, Evans BW (2010) Abbreviations for names of rock-forming minerals. Am Mineral 95:185–187
Whitney DL, Teyssier C, Seaton NCA, Fornash KF (2014) Petrofabrics of high-pressure rocks exhumed at the slab-mantle interface from the "point of no return" in a subduction zone (Sivrihisar, Turkey). Tectonics 33:2315–2341
Zhang RY, Liou JG (1997) Partial transformation of gabbro to coesite-bearing eclogite from Yangkou, the Sulu terrane, eastern China. J Metamorph Geol 15:183–202